

# Solar Neutrinos: Status and Prospects

W.C. Haxton,<sup>1</sup> R.G. Hamish Robertson,<sup>2</sup>  
and Aldo M. Serenelli<sup>3</sup>

<sup>1</sup>Department of Physics, University of California, Berkeley, and Nuclear Science Division, Lawrence Berkeley National Laboratory, Berkeley, California 94720-7300; email: haxton@berkeley.edu

<sup>2</sup>Department of Physics, University of Washington, and Center for Experimental Nuclear Physics and Astrophysics, Seattle, Washington 98195; email: rghr@u.washington.edu

<sup>3</sup>Instituto de Ciencias del Espacio (CSIC-IEEC), Facultad de Ciencias, 08193 Bellaterra, Spain and Max Planck Institute for Astrophysics, Garching, D-85471, Germany; email: aldoses@ice.csic.es

Annu. Rev. Astron. Astrophys. 2013. 51:21–61

First published online as a Review in Advance on June 27, 2013

The *Annual Review of Astronomy and Astrophysics* is online at [astro.annualreviews.org](http://astro.annualreviews.org)

This article's doi:  
10.1146/annurev-astro-081811-125539

Copyright © 2013 by Annual Reviews.  
All rights reserved

## Keywords

solar neutrinos, neutrino oscillations, solar models, helioseismology, nuclear astrophysics, metal abundances

## Abstract

We describe the current status of solar neutrino measurements and of the theory—both neutrino physics and solar astrophysics—employed in interpreting measurements. Important recent developments include Super-Kamiokande's determination of the  $\nu - e$  elastic scattering rate for  $^8\text{B}$  neutrinos to 3%; the latest Sudbury Neutrino Observatory (SNO) global analysis in which the inclusion of low-energy data from SNO I and II significantly narrowed the range of allowed values for the neutrino mixing angle  $\theta_{12}$ ; Borexino results for both the  $^7\text{Be}$  and proton-electron-proton (pep) neutrino fluxes, the first direct measurements constraining the rate of proton-proton (pp) I and pp II burning in the Sun; global reanalyses of solar neutrino data that take into account new reactor results on  $\theta_{13}$ ; a new decadal evaluation of the nuclear physics of the pp chain and CNO cycle defining best values and uncertainties in the nuclear microphysics input to solar models; recognition of an emerging discrepancy between two tests of solar metallicity, helioseismological mappings of the sound speed in the solar interior, and analyses of the metal photoabsorption lines based on our best current description of the Sun's photosphere; a new round of standard solar model calculations optimized to agree either with helioseismology or with the new photospheric analysis; and, motivated by the solar abundance problem, the development of nonstandard, accreting solar models, in order to investigate possible consequences of the metal segregation that occurred in the proto-solar disk. We review this progress and describe how new experiments such as SNO+ could help us further exploit neutrinos as a unique probe of stellar interiors.

## 1. INTRODUCTION

In 1958, Holmgren & Johnston (1958, 1959) found that the cross section for  ${}^3\text{He} + {}^4\text{He} \rightarrow {}^7\text{Be} + \gamma$  was about 1,000 times larger than anticipated, so that in addition to the simplest  ${}^3\text{He} + {}^3\text{He} \rightarrow {}^4\text{He} + 2\text{p}$  proton-proton (pp) I termination of the pp chain (see **Figure 1**), there might be significant branches to the pp II and pp III cycles and, thus, significant fluxes of  ${}^7\text{Be}$  and  ${}^8\text{B}$  solar neutrinos. Despite the uncertainties that existed in 1958—the solar core temperature was poorly constrained by theory, and other nuclear physics important to the pp chain had not been resolved—both Cameron (1958) and Fowler (1958) pointed out that it might be possible to detect solar neutrinos using a radiochemical method Ray Davis had developed at Brookhaven (Davis 1955). Although the endpoint of the main source of neutrinos from the pp I cycle,  $\text{p} + \text{p} \rightarrow \text{d} + \text{e}^+ + \nu_e$ , is below the 811-keV threshold for  $\nu_e + {}^{37}\text{Cl} \rightarrow {}^{37}\text{Ar} + \text{e}^-$ , most  ${}^7\text{Be}$  and  ${}^8\text{B}$  neutrinos are sufficiently energetic to drive this reaction. In 1962 Fowler organized a team of young Caltech researchers—John Bahcall, Icko Iben, and Dick Sears—to begin the development of a solar model to more accurately predict the central temperature of the Sun and to estimate the rates of neutrino-producing reactions (Bahcall et al. 1963). The history of these early developments is summarized in several sources (Bahcall & Davis 1982, Haxton 2010, Lande 2010). By early 1964, following significant advances in the solar model and in the understanding of the nuclear physics of the pp chain and the  ${}^{37}\text{Cl}(\nu_e, \text{e}^-){}^{37}\text{Ar}$  reaction, Davis (1964) and Bahcall (1964) concluded that a measurement of solar neutrinos would be possible, were Davis to mount a detector 100 times larger than that he built at Brookhaven, in a site sufficiently deep to reduce backgrounds from high-energy cosmic-ray muons to an acceptable level. In April 1968, Davis, Harmer & Hoffman (1968) announced an upper bound on the solar neutrino capture rate for  ${}^{37}\text{Cl}$  of 3 SNU ( $1 \text{ SNU} = 10^{-36}$  captures target $^{-1}$

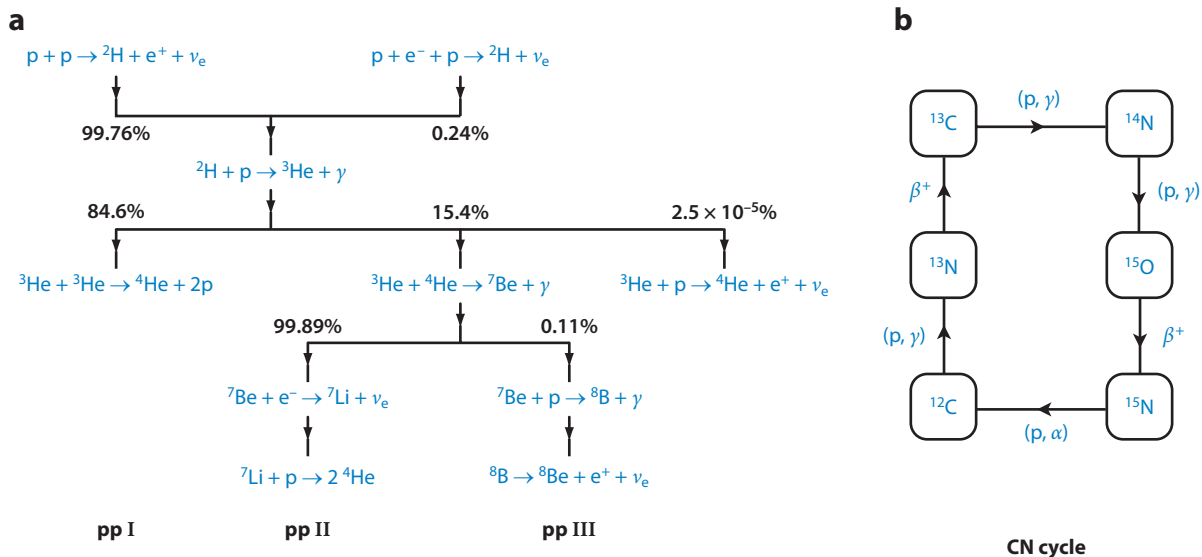


**Figure 1**

(a) The three principal cycles comprising the proton-proton (pp) chain (pp I, pp II, and pp III), the associated neutrinos that “tag” each of the three branches, and the theoretical branching percentages defining the relative rates of competing reactions (GS98-SFII SSM). Also shown is the minor branch  ${}^3\text{He} + \text{p} \rightarrow {}^4\text{He} + \text{e}^+ + \nu_e$ , which generates the most energetic neutrinos. (b) The CN I cycle, which produces the  ${}^{13}\text{N}$  and  ${}^{15}\text{O}$  neutrinos.

atom  $s^{-1}$ ), based on the initial running of a 100,000-gallon  $C_2Cl_4$  detector that the collaborators had constructed on the 4,850-ft level of the Homestake gold mine, in Lead, South Dakota.

This upper bound, nearly a factor of three below the rate predicted by the Bahcall, Bahcall & Shaviv (1968) standard solar model (SSM), began a controversy that took 30 years to resolve. With great prescience, Pontecorvo (1967) proposed the phenomenon of neutrino oscillation as a way of explaining a low result. Nevertheless, twenty of those years passed without independent confirmation of the Davis result: Because the Cl rate was a fraction of a count per day in 0.6 kton of organic liquid, other technologies with comparable sensitivity were not easily developed. Because the Davis experiment was sensitive to a flux of neutrinos that varies steeply with the solar core temperature [ $\phi(^8B) \sim T_C^{22}$ ; Bahcall 1989], the result could be accommodated without endowing neutrinos with new properties by a variety of possible changes in the SSM, resulting in the net effect of reducing  $T_C$  by  $\sim 5\%$ . But as additional constraints on solar neutrino fluxes were established by the Kamiokande Collab., Hirata et al. (1989), SAGE Collab., Abdurashitov et al. (1994), and GALLEX Collab., Anselmann et al. (1994), a more detailed pattern of fluxes emerged that was not easily reconciled with any astrophysical solution. In contrast, with the discovery of the Mikheyev-Smirnov-Wolfenstein (MSW) mechanism (Mikheyev & Smirnov 1985, 1986; Wolfenstein 1978a,b), it became apparent that neutrino oscillations augmented by matter effects could account for the observations, even for a small mixing angle. The conclusion of an Annual Reviews article from this period (Haxton 1995) captures the sense of excitement that with new experiments, a resolution of the solar neutrino problem was near.

In 1998, following a series of results from proton-decay and magnetic-monopole searches that reported unexpectedly low fluxes of atmospheric muon neutrinos (Kajita & Totsuka 2001),  $\nu_\mu \rightarrow \nu_\tau$  vacuum neutrino oscillations were convincingly demonstrated in the zenith-angle dependence of neutrino fluxes (Super-Kamiokande Collab., Y. Fukuda et al. 1998). Although this result did not directly constrain the  $\nu_e$ s produced by the Sun, the discovery was a game changer, confirming the existence of the phenomenon suggested by Pontecorvo (1967). Direct evidence that neutrino flavor conversion indeed explained the solar neutrino problem came when the Sudbury Neutrino Observatory (SNO) collaboration (SNO Collab., Ahmad et al. 2001, 2002) measured both the  $\nu_e$  and heavy-flavor components of the  $^8B$  solar neutrino flux arriving at Earth, utilizing three detection channels with different sensitivities to charged currents (CCs) and neutral currents (NCs). The total flux of neutrinos (summed over flavors) was found to be in good agreement with the SSM prediction, but some two-thirds of the neutrinos arrived at Earth in heavy flavors. The energy-dependent effect of matter on solar neutrino oscillations explains the differential suppression of the pp,  $^7Be$ , and  $^8B$  fluxes deduced from previous experiments. In the neutrino-oscillation description, three different sets of parameters were consistent with SNO data, and it was not until 2002 when the KamLAND Collab., Eguchi et al. (2003) found the same oscillation phenomenon in terrestrial antineutrinos from distant nuclear reactors that a unique choice could be made.

This review summarizes the basic physics of solar neutrinos, the work that led to the discoveries noted above, and the impact of recent and ongoing solar neutrino experiments on astrophysics and weak interactions, including the following:

- Completion of phase III of the Super-Kamiokande experiment (Super-Kamiokande Collab., Abe et al. 2011) and preliminary results from Super-Kamiokande IV's low-threshold running (Super-Kamiokande Collab., Smy et al. 2013);
- SNO's combined analysis of all three SNO phases (SNO Collab., Aharmim et al. 2012) and the collaboration's low-energy analysis of the data from SNO I and II (SNO Collab., Aharmim et al. 2010);

- Borexino’s achievement of a 5% measurement of the  ${}^7\text{Be}$  flux, an initial result for the proton-electron-proton (pep) flux, and a limit on the CN neutrino contribution (Borexino Collab., Bellini et al. 2011, 2012a); and
- Daya Bay, Reno, and Double Chooz measurements of  $\theta_{13}$ , impacting global analyses of solar neutrino data (Daya Bay Collab., An et al. 2012; Double Chooz Collab., Abe et al. 2012; RENO Collab., Ahn et al. 2012).

In addition, a comprehensive survey of the nuclear physics of the pp chain and CNO cycle has been completed, yielding a new set of best values and uncertainties for the nuclear rates (Adelberger et al. 2011). The sound speed throughout most of the Sun’s interior has been extracted from helioseismology to an accuracy of  $\sim 0.1\%$ , providing a stringent check on SSM predictions. More sophisticated 3D models of the solar atmosphere have been developed, not only significantly improving the agreement between predicted and observed absorption line-shapes and the consistency of abundance determinations from different atomic and molecular lines (Asplund et al. 2009), but also yielding a photospheric metal abundance  $\sim 30\%$  below 1D values, leading to a conflict between SSMs employing the new abundances and solar parameters deduced from helioseismology. The SSM has been updated for the new nuclear reaction rates and alternative metallicities, and nonstandard models have been developed to explore accretion as a possible solution to the solar abundance problem (Serenelli et al. 2009; Serenelli, Haxton & Peña-Garay 2011).

For three decades solar neutrino physics was defined by an incomplete knowledge of the neutrino fluxes and shortcomings in our understanding of neutrino flavor physics. We are now starting a new period, in which precise spectroscopy of the full spectrum of solar neutrinos is possible and a clearer understanding of weak interactions has been obtained from a combination of astrophysical, reactor, and accelerator experiments. On one hand, this returns us to the roots of solar neutrino physics: With weak interaction uncertainties removed, solar neutrinos can be used to probe possible limitations in the SSM—such as uncertainties in the Sun’s initial composition and the absence of *ab initio* treatments of mixing and other 3D physics, including rotation and magnetic fields. On the other hand, the neutrinos coming from the Sun remain important to fundamental physics: the spectral shapes and fluxes of the various sources are known rather precisely, and low-energy neutrinos react with targets rather simply, giving us confidence that we can interpret measurements. Thus, this review also considers the continuing role solar neutrinos could play in further constraining the Pontecorvo–Maki–Nakagawa–Sakata (PMNS) neutrino mass matrix and in probing matter effects and other environmental neutrino phenomena.

## 2. THE STANDARD SOLAR MODEL AND ITS NUCLEAR AND NEUTRINO PHYSICS

### 2.1. The Standard Solar Model

Solar models trace the evolution of the Sun from its beginning—when the collapse of the presolar gas cloud was halted by the turn-on of thermonuclear reactions—to today, thereby predicting contemporary solar properties such as the composition, temperature, pressure, and sound-speed profiles and the neutrino fluxes. SSMs are based on the following four assumptions (Bahcall 1989):

- The Sun burns in hydrostatic equilibrium, maintaining a local balance between the gravitation force and pressure gradient. To implement this condition, an equation of state (EoS) is needed. As the hydrogen and helium in the Sun’s core are nearly completely ionized, an ideal gas EoS with corrections for incomplete ionization of metals, radiation

pressure, and screening is thought to provide a good approximation to the EoS (Bahcall 1989). Helioseismic inversions of solar p-mode frequencies have provided important tests of the associated theory (Elliott & Kosovichev 1998).

- The mechanisms for energy transport are radiation and convection. The inner portion of the Sun—98% by mass or about 71% by radius—is radiative. In order to describe radiative transport, the opacity must be known as a function of temperature, density, and composition. In addition to elementary processes such as Thomson scattering off electrons and inverse bremsstrahlung off fully ionized hydrogen and helium, more complex processes such as bound-free scattering off metals are important contributors to the opacity in the Sun’s central regions. Thus, modern opacity tables like OPAL (Rogers & Nayfonov 2002) are based on detailed atomic input. Changes in opacity influence important helioseismic properties such as the sound speed and the location of the convective zone boundary. In the Sun’s outer envelope, where the radiative gradient is larger, convection dominates the energy transport. SSM convection is modeled through mixing length theory, in which volume elements are transported radially over a characteristic distance determined empirically in the model, but typically on the order of the pressure scale height.
- The Sun produces its energy by fusing protons into  ${}^4\text{He}$ ,



via the pp chain (~99%) and CN cycle (~1%). The nuclear cross sections are taken from experiment or, if that is impractical, from theory: The associated laboratory astrophysics is challenging because reaction rates are needed for energies well below the Coulomb barrier. Thus, laboratory measurements are generally made at higher energies, with theory guiding the extrapolations to the solar Gamow window.

- Boundary conditions include the modern Sun’s mass, age, radius  $R_\odot$ , and luminosity  $L_\odot$ . The presolar composition is divided into hydrogen  $X_{\text{ini}}$ , helium  $Y_{\text{ini}}$ , and metals  $Z_{\text{ini}}$ , with  $X_{\text{ini}} + Y_{\text{ini}} + Z_{\text{ini}} = 1$ . Relative metal abundances can be determined from a combination of photospheric (determined from analyses of absorption lines) and meteoritic (for refractory elements) abundances and are generally assumed to have remained constant since the Sun formed. The photospheric abundances and the assumption of a homogeneous zero-age Sun then constrain the Sun’s initial core composition: One can equate the presolar core metallicity  $Z_{\text{ini}}$  to the present photospheric  $Z_S$ , corrected for the effects of diffusion over the Sun’s lifetime. Finally  $Y_{\text{ini}}$  and the mixing length  $\alpha_{\text{MLT}}$  are determined interactively by demanding that  $L_\odot$  and  $R_\odot$  are produced after 4.6 Gyr of burning.

The resulting model is dynamic. The luminosity of the Sun increases by ~40% over the solar lifetime: Helium synthesis alters the mean molecular weight and opacity in the core, requiring a response in  $T_C$ . The ratio of pp I/pp II/pp III burning changes, with the fraction of energy produced through the more temperature-sensitive pp II and pp III branches increasing. The  ${}^8\text{B}$  neutrino flux for the pp III cycle has an exceedingly sharp growth  $\sim e^{t/\tau}$ , where  $\tau \sim 0.9$  Gyr. Composition gradients are created as the pp chain burns to equilibrium. An interesting example is the solar core  ${}^3\text{He}$  abundance, which rises steeply with increasing radius,  $X_3 \propto T^{-6}$ , throughout the region where pp-chain equilibrium has been reached. The  ${}^3\text{He}$  abundance gradient was proposed as a potential trigger for periodic mixing of the core in the “solar spoon” (Dilke & Gough 1972). Metals are rearranged: In the first  $10^8$  years of main-sequence burning most of the carbon in the Sun’s central core is converted to nitrogen, building up the core abundance of  ${}^{14}\text{N}$ . Because they have a smaller charge-to-mass ratio than hydrogen,  ${}^4\text{He}$  and metals slowly diffuse toward the core—another source of composition gradients that affect contemporary observables like helioseismology.

**Table 1** Standard solar model characteristics are compared to helioseismic values, as determined by Basu & Antia (1997, 2004)

Property <sup>a</sup>	GS98-SFII	AGSS09-SFII	Solar
$(Z/X)_S$	0.0229	0.0178	–
$Z_S$	0.0170	0.0134	–
$Y_S$	0.2429	0.2319	$0.2485 \pm 0.0035$
$R_{CZ}/R_\odot$	0.7124	0.7231	$0.713 \pm 0.001$
$\langle \delta c/c \rangle$	0.0009	0.0037	0.0
$Z_C$	0.0200	0.0159	–
$Y_C$	0.6333	0.6222	–
$Z_{ini}$	0.0187	0.0149	–
$Y_{ini}$	0.2724	0.2620	–

<sup>a</sup>X, Y, and Z are the mass fractions in H, He, and metals, respectively. The subscripts S, C, and ini denote current photospheric, current core, and zero-age values, respectively.  $R_{CZ}$  is the radius to the convective zone, and  $\langle \delta c/c \rangle$  is the average fractional discrepancy in the sound speed, relative to helioseismic values.

Properties of two SSMs we use in this review are listed in **Table 1**. The models differ in the values assumed for the photospheric metallicity  $Z_S$ , with the GS98-SFII SSM being more metal rich than the AGSS09-SFII SSM. The table gives the model photospheric helium  $Y_S$  and metal  $Z_S$  abundances, the radius of the convective zone  $R_{CZ}$ , the mean deviation of the sound speed  $\langle \delta c/c \rangle$  from the helioseismic profile, the core helium and heavy element abundances  $Y_C$  and  $Z_C$ , and the Sun’s presolar abundances  $Y_{ini}$  and  $Z_{ini}$ .

## 2.2. The Proton-Proton Chain and Carbon-Nitrogen Cycle

Approximately 80% of observed stars lie along a path in the Hertzsprung–Russell diagram characterized by energy generation through proton burning. The Sun provides a unique opportunity to test our understanding of main-sequence stars, as we can compare model predictions to solar properties that are precisely known. This has inspired a great deal of laboratory work to reduce uncertainties in atomic opacities and nuclear cross sections—key SSM input parameters—so that we can assess the reliability of the more fundamental solar physics and weak interactions aspects of the model.

In lower mass hydrogen-burning stars,  ${}^4\text{He}$  is synthesized primarily through the pp-chain nuclear reactions shown in **Figure 1a**. The rates of the pp I, pp II, and pp III cycles comprising the pp chain can be determined from the fluxes of the pp/pep,  ${}^7\text{Be}$ , and  ${}^8\text{B}$  neutrinos produced by those cycles. As the relative rates are very sensitive to  $T_C$ , the neutrino fluxes are a sensitive thermometer for the solar core, provided the associated nuclear physics is under control.

Rates depend on the quantity  $\langle \sigma v \rangle_{\text{MB}}$ , where  $v$  is the relative velocity between two colliding nuclei,  $\sigma$  is the cross section, and  $\langle \rangle_{\text{MB}}$  denotes an average over the Maxwell-Boltzmann relative velocity distribution in the solar plasma. The optimal energy for a solar reaction, called the Gamow peak, is determined from the competition between a cross section that rises rapidly as the energy climbs the Coulomb barrier and a relative-velocity distribution that declines rapidly on the Maxwell-Boltzmann tail. Two pp I-cycle reactions,  $d + p$  and  ${}^3\text{He} + {}^3\text{He}$ , have been measured in their Gamow peaks. Data were obtained down to 2.5 and 16 keV, respectively, at LUNA (Laboratory for Underground Nuclear Astrophysics), Gran Sasso’s low-background facility for nuclear astrophysics (Bonetti et al. 1999, Brogini et al. 2010). For other pp-chain

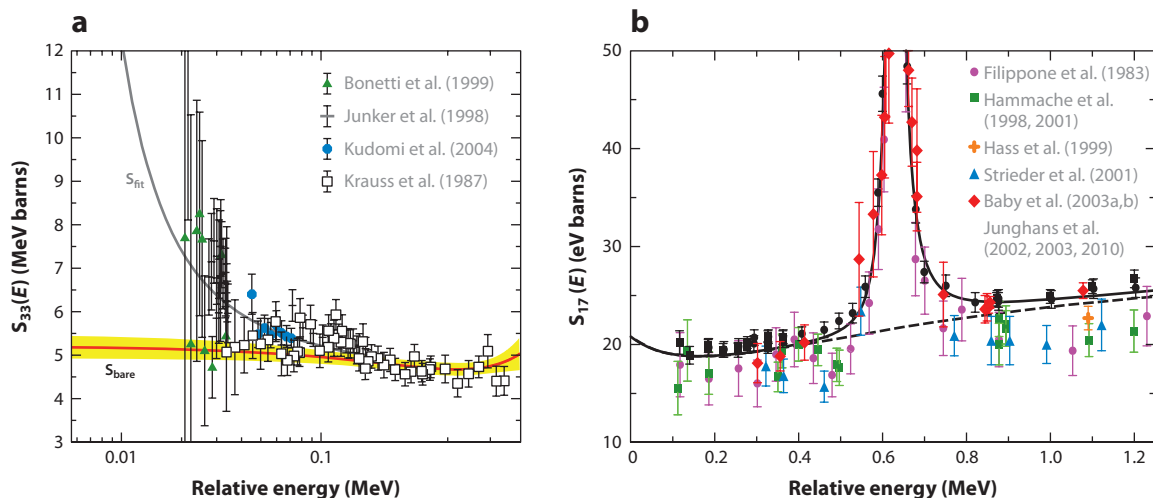


**Figure 2**

(a) The data, the best quadratic + screening result for  $S_{33}(E)$ , and the deduced best quadratic fit (red line) and allowed range (yellow band) for  $S_{33}^{\text{bare}}$ . (b)  $S_{17}(E)$  versus center-of-mass energy  $E$ , for  $E \leq 1,250$  keV. Data points are shown with total errors, including systematic errors. The dashed line is based on a theoretical calculation, scaled to fit the data. See Solar Fusion II and Broggini et al. (2010) for references and details.

reactions, direct measurements are not currently possible because of the severity of the Coulomb suppression. Instead, measurements must be made at higher energies, then extrapolated to solar energies using nuclear models to predict the cross section shape.

Such extrapolations are usually performed by using the S-factor,

$$\sigma(E) = \frac{S(E)}{E} \exp[-2\pi\eta(E)], \quad (2)$$

which removes from the cross section the rapid energy dependence associated with the s-wave interaction of point nuclei. Here the Sommerfeld parameter is  $\eta(E) = Z_1 Z_2 \alpha / v$ , with  $Z_1$  and  $Z_2$  representing the ion charges, the relative velocity is  $v = \sqrt{2E/\mu}$  (where  $\mu$  is the reduced mass), and  $\alpha$  is the fine structure constant ( $\hbar = c = 1$ ). The remaining nuclear physics (including effects of finite nuclear size, higher partial waves, antisymmetrization, and any atomic screening effects not otherwise explicitly treated) is then isolated in  $S(E)$ , the function used in extrapolations because of its gentler dependence on  $E$ . In solar applications  $S(E)$  is frequently approximated by its zero-energy value  $S(0)$  and corrections determined by its first and second derivatives,  $S'(0)$  and  $S''(0)$ .

The recent review by Adelberger et al. (2011) (Solar Fusion II) details the data and theory issues affecting our understanding of solar cross sections. Uncertain S-factors remain one of the key limitations in SSM neutrino flux predictions. **Figure 2a,b** gives the Solar Fusion II summaries for  ${}^3\text{He} + {}^3\text{He} \rightarrow {}^4\text{He} + 2p$  and  ${}^7\text{Be} + p \rightarrow {}^8\text{B} + \gamma$ , respectively. Although measurements for the first reaction cover the solar energies of interest, the screening environment of a terrestrial target (neutral atoms) differs from that at the center of the Sun (ionized  ${}^3\text{He}$ ). It is apparent from **Figure 2** that the theoretical screening correction is significant.

The reaction  ${}^7\text{Be}(p, \gamma) {}^8\text{B}$  (**Figure 2b**) feeds the pp III cycle that produces the  ${}^8\text{B}$  neutrinos measured by SNO and Super-Kamiokande. This reaction was considered the most uncertain in the pp chain when these detectors began operations, with only a single data set considered sufficiently reliable and well documented for inclusion in an S-factor determination

**Table 2** Standard solar model (SSM) neutrino fluxes from the GS98-SFII and AGSS09-SFII SSMs, with associated uncertainties (averaging over asymmetric uncertainties)<sup>a</sup>

$\nu$ flux	$E_{\nu}^{\max}$ (MeV)	GS98-SFII	AGSS09-SFII	Solar	Units
$p + p \rightarrow {}^2\text{H} + e^+ + \nu$	0.42	$5.98(1 \pm 0.006)$	$6.03(1 \pm 0.006)$	$6.05(1_{-0.011}^{+0.003})$	$10^{10} \text{ cm}^{-2} \text{ s}^{-1}$
$p + e^- + p \rightarrow {}^2\text{H} + \nu$	1.44	$1.44(1 \pm 0.012)$	$1.47(1 \pm 0.012)$	$1.46(1_{-0.014}^{+0.010})$	$10^8 \text{ cm}^{-2} \text{ s}^{-1}$
${}^7\text{Be} + e^- \rightarrow {}^7\text{Li} + \nu$	0.86 (90%)	$5.00(1 \pm 0.07)$	$4.56(1 \pm 0.07)$	$4.82(1_{-0.04}^{+0.05})$	$10^9 \text{ cm}^{-2} \text{ s}^{-1}$
	0.38 (10%)				
${}^8\text{B} \rightarrow {}^8\text{Be} + e^+ + \nu$	$\sim 15$	$5.58(1 \pm 0.14)$	$4.59(1 \pm 0.14)$	$5.00(1 \pm 0.03)$	$10^6 \text{ cm}^{-2} \text{ s}^{-1}$
${}^3\text{He} + p \rightarrow {}^4\text{He} + e^+ + \nu$	18.77	$8.04(1 \pm 0.30)$	$8.31(1 \pm 0.30)$	—	$10^3 \text{ cm}^{-2} \text{ s}^{-1}$
${}^{13}\text{N} \rightarrow {}^{13}\text{C} + e^+ + \nu$	1.20	$2.96(1 \pm 0.14)$	$2.17(1 \pm 0.14)$	$\leq 6.7$	$10^8 \text{ cm}^{-2} \text{ s}^{-1}$
${}^{15}\text{O} \rightarrow {}^{15}\text{N} + e^+ + \nu$	1.73	$2.23(1 \pm 0.15)$	$1.56(1 \pm 0.15)$	$\leq 3.2$	$10^8 \text{ cm}^{-2} \text{ s}^{-1}$
${}^{17}\text{F} \rightarrow {}^{17}\text{O} + e^+ + \nu$	1.74	$5.52(1 \pm 0.17)$	$3.40(1 \pm 0.16)$	$\leq 59$	$10^6 \text{ cm}^{-2} \text{ s}^{-1}$
$\chi^2/P^{\text{agr}}$		3.5/90%	3.4/90%		

<sup>a</sup>The solar values come from a luminosity-constrained analysis of all available data by the Borexino Collaboration.

(Adelberger et al. 1998). Four new, high-quality data sets were available for the Solar Fusion II evaluation, yielding  $S_{17}(0) = 20.8 \pm 0.7$  (expt)  $\pm 1.4$ (theor). The dominant error is now the theoretical extrapolation to the Gamow peak.

The CN I cycle, illustrated in **Figure 1b**, is typically the dominant mode for hydrogen burning in massive main-sequence stars, where core temperatures exceed those of the Sun. Unlike the pp chain, the CN cycle depends on pre-existing metals to catalyze a series of (p,  $\gamma$ ) and (p,  $\alpha$ ) reactions, leading in sum to Equation 1. Thus, the CN cycle is (in most settings) a secondary process, dependent on the star's metallicity. In the Sun the CN cycle converts C to N as it seeks equilibrium. Equilibrium has been reached only in the most central regions of the core, where  $T \gtrsim 1.33 \times 10^7$  K. Outside this region, the bottleneck reaction  ${}^{14}\text{N}(p, \gamma)$  inhibits cycling. Thus, throughout most of the cooler regions of the core, very little CN-cycle burning takes place: Presolar  ${}^{12}\text{C}$  has already been converted to  ${}^{14}\text{N}$ , but little  ${}^{14}\text{N}$  is being consumed. Still further outward, where  $T \lesssim 10^7$  K, the  ${}^{12}\text{C}$  lifetime is comparable to the solar age. This is the region in the contemporary Sun where presolar  ${}^{12}\text{C}$  is being burned. Thus, CN-cycle neutrinos, produced in the  $\beta^+$  decay of  ${}^{15}\text{O}$  and  ${}^{13}\text{N}$ , come from two distinct regions. Deep in the solar core equal numbers of  ${}^{15}\text{O}$  and  ${}^{13}\text{N}$  neutrinos are produced in equilibrium burning, whereas in the distant cool outer regions of the core, only  ${}^{13}\text{N}$  neutrinos are produced.

### 2.3. Solar Neutrino Fluxes

The main neutrino-producing reactions of the pp chain and CN cycle are summarized in **Table 2**. Four of the five  $\beta$  decay reactions produce neutrino spectra with allowed shapes and endpoints given by  $E_{\nu}^{\max}$ . In the fifth, the decay of  ${}^8\text{B}$ , the  ${}^8\text{Be}$  final state is a broad ( $\sim 2$ -MeV) resonance. Because the profile of this resonance is known, the associated small deviations from an allowed spectrum can be calculated. In addition to the main pp/pep,  ${}^7\text{Be}$ , and  ${}^8\text{B}$  neutrinos, a fourth source from a weak side-branch of the pp chain, the hep or  ${}^3\text{He} + p$  neutrinos, is shown in **Figure 1**. These are the most energetic neutrinos produced by the Sun ( $E_{\nu}^{\max} \sim 18.77$  MeV) and, thus, may be observable in SNO and Super-Kamiokande event distributions because they populate energy bins above the  ${}^8\text{B}$  neutrino endpoint. The two electron-capture (EC) reactions,  $p + e^- + p$  and  ${}^7\text{Be} + e^-$ , produce line sources of neutrinos of energy  $E_{\nu}^{\max}$  broadened by thermal effects. There are two lines associated with  ${}^7\text{Be}$  EC, as  $\sim 10\%$  of the captures populate the first excited state in  ${}^7\text{Li}$ .

The pp I, pp II, and pp III contributions to solar energy generation can be determined from measurements of the pp/pep,  ${}^7\text{Be}$ , and  ${}^8\text{B}$  neutrino fluxes. As we discuss in the next section below, the  ${}^7\text{Be}$  and  ${}^8\text{B}$  fluxes are now quite well known, whereas the first measurement of pep neutrinos was very recently announced. The “solar values” of **Table 2** come from the Borexino Collaboration (private communication), which updated an analysis by Bahcall & Peña-Garay (2003), combining  ${}^8\text{B}$ ,  ${}^7\text{Be}$ , and pep flux measurements (available as of March 2011) with the solar luminosity constraint in order to fix the principal pp-chain fluxes. That is, the sum of the rates for the pp I, pp II, and pp III cycles, weighted by the energy each cycle deposits in the Sun, is fixed by the photon luminosity. Consequently, the fluxes labeled as solar values are not strictly measured ones, but derived assuming a steady-state Sun.

**Table 2** also gives fluxes for two solar models, reflecting the metallicity uncertainties mentioned previously. The first model uses abundances for volatile elements that were obtained from an absorption line analysis in which the photosphere was treated in 1D, yielding  $(Z/X)_S = 0.0229$  (Grevesse & Sauval 1998). As Solar Fusion II cross sections are used as well, this model is denoted as GS98-SFII. The second, denoted as AGSS09-SFII, takes abundances from a 3D photospheric model, yielding  $(Z/X)_S = 0.0178$  (Asplund et al. 2009). The solar core is sensitive to metallicity because free-bound/bound-free transitions in metals are an important contributor to the opacity. A low-metallicity Sun, as in model AGSS09-SFII, produces a somewhat cooler core (by  $\sim 1\%$ ) and, thus, lower fluxes of temperature-sensitive neutrinos, such as those from  ${}^8\text{B}$   $\beta$  decay.

The SSM fluxes for the CN I cycle  $\beta$  decays of  ${}^{13}\text{N}$  and  ${}^{15}\text{O}$  and the CNO II cycle decay of  ${}^{17}\text{F}$  are also shown in **Table 2**. Despite the minor role the CN cycle plays in solar energy generation, these fluxes are significant. The excess in the flux of  ${}^{13}\text{N}$  neutrinos relative to  ${}^{15}\text{O}$  neutrinos in **Table 2** is a consequence of the out-of-equilibrium burning of the CN cycle discussed above.

The SSM uncertainties given in **Table 1** are generated from the uncertainties assigned to approximately 20 model input parameters, denoted by  $\beta_j$ . These include the solar age, present-day luminosity, opacities, the diffusion constant, the S-factors for the pp chain and CN cycle, and the various metal abundances (key elements such as C, N, O, Ne, Mg, Si, S, Ar, and Fe). The consequences of input SSM uncertainties on observables are typically parameterized through logarithmic partial derivatives  $\alpha(i, j)$ , determined by calculating the SSM response to variations in the  $\beta_j$ . For example, in the case of the neutrino fluxes  $\phi_i$ , the

$$\alpha(i, j) \equiv \frac{\partial \ln[\phi_i/\phi_i(0)]}{\partial \ln[\beta_j/\beta_j(0)]} \quad (3)$$

can be found in the SSM updates by Peña-Garay & Serenelli (2008) and Serenelli (2010). Here,  $\phi_i(0)$  and  $\beta_j(0)$  denote the SSM best values.

The partial derivatives define the power-law dependencies of neutrino fluxes with respect to the SSM best-value prediction  $\phi_i(0)$ ,

$$\phi_i \sim \phi_i(0) \prod_{j=1}^{19} \left[ \frac{\beta_j}{\beta_j(0)} \right]^{\alpha(i,j)} = \phi_i(0) \prod_{j=1}^{19} [1 + \delta\beta_j]^{\alpha(i,j)}, \quad (4)$$

where  $\delta\beta_j \equiv \Delta\beta_j/\beta_j(0)$  is the fractional uncertainty of input parameter  $\beta_j$  with respect to its SSM best value. As this expression separates the impact of SSM parameter variations on  $\phi_i$  into a solar piece [the infinitesimal SSM response described by  $\alpha(i, j)$ ] and a laboratory or theory piece (the estimated uncertainty  $\delta\beta_j$  of an input parameter), the effects of parameter variations can be explored without repeating SSM calculations.

The solar abundance problem is characterized by large systematic differences in the SSM  $\beta_j$  for key abundances. Consequently, the differences in the GS98-SFII and AGSS09-SFII SSM neutrino flux predictions of **Table 2** exceed their respective internal statistical uncertainties in

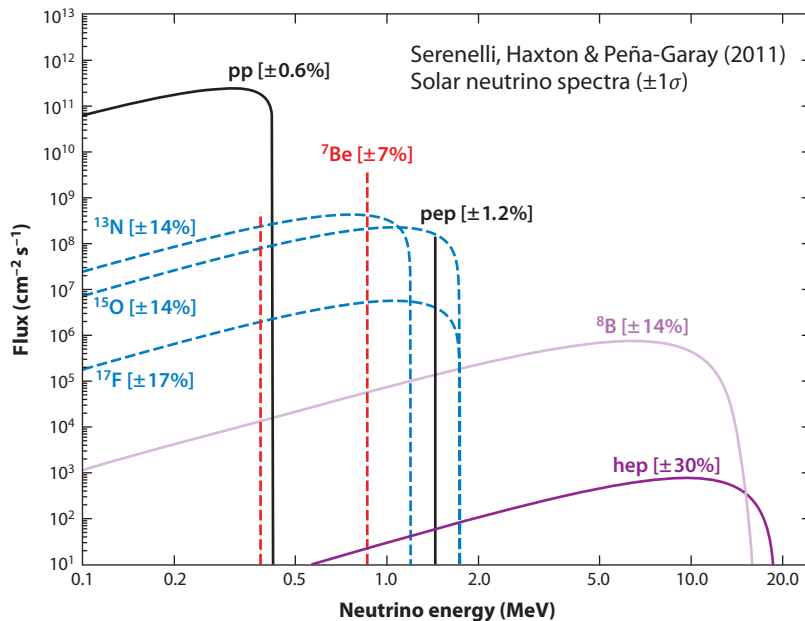


**Figure 3**

The solar neutrino spectrum along with the standard solar model uncertainties (Serenelli, Haxton & Peña-Garay 2011). A weak branch from the  $\beta$  decay of  $^{17}\text{F}$  that contributes from the CNII cycle is included. For the continuous sources flux densities are shown: one must integrate over  $E$  to get fluxes in the indicated units. Abbreviations: hep,  $^3\text{He} + \text{p}$ ; pep, proton-electron-proton; pp, proton-proton.

several cases. The table summarizes key helioseismic predictions of both models, with the low- $Z$  AGSS09-SFII SSM predictions being in significantly poorer agreement with the data.

The spectrum of solar neutrinos emitted by the Sun is shown in **Figure 3**. This familiar figure is somewhat idealized: It includes competing  $\beta$  decay and EC branches for the  $\text{p} + \text{p}$  reaction, but omits the EC lines that accompany the other  $\beta$  decay reactions of **Table 2**. The EC branching ratio increases with increasing  $Z$  and decreasing  $Q$  values. Thus, among the omitted cases, EC is most significant for the CNO cycle reactions, where rate estimates were made by Stonehill, Formaggio & Robertson (2004). The EC lines shown in the figure are in fact thermally broadened because they occur in a plasma. Finally, at energies  $\lesssim 10$  keV below the scale of **Figure 3**, there is a contribution from neutrino pairs of all flavors produced thermally in the solar core (Haxton & Lin 2000): Though the flux of these neutrinos is modest, the peak flux density of  $\sim 10^9 \text{ cm}^{-2} \text{ s}^{-1} \text{ MeV}^{-1}$  exceeds that of all solar  $\beta$  decay sources except for the pp neutrinos.

In the following sections, we describe how measurements of the various sources can provide unique information on the structure and composition of the Sun, and on the properties of neutrinos, including how those properties depend on the surrounding environment.

### 3. EXPERIMENTS: NEUTRINOS AND HELIOSEISMOLOGY

The SSM is a model of the Sun's interior structure, rather than the more complicated behavior of the convective envelope. The two main tools by which we can probe the solar interior and, thus, test the validity of the SSM are neutrino spectroscopy and helioseismology. Neutrino fluxes are sensitive to core temperature—a property that responds to changes in the opacity and

composition—and to nuclear cross sections. Helioseismic maps of the sound speed throughout much of the solar interior have achieved accuracy of a few parts in 1,000, constraining the solar density and pressure profiles, and determining rather precisely the boundary between the Sun’s radiative core and convective envelope.

### 3.1. Neutrino Spectroscopy: Early Experiments

Here we describe the chlorine, Kamiokande II/III, and gallium experiments. By the early 1990s, the data from these experiments suggested a pattern of neutrino fluxes not easily reconciled with the SSM, stimulating the construction of a new generation of large active detectors.

**3.1.1. The chlorine experiment.** Radiochemical detection of neutrinos by  $^{37}\text{Cl}(\nu_e, e^-) ^{37}\text{Ar}$  was suggested by Pontecorvo (1946) and explored in more detail by Alvarez (1949), who was interested in the possibility of a reactor neutrino experiment to detect a Majorana neutrino. Ray Davis’s efforts to develop a practical detector began with his Brookhaven experiment (Davis 1955), which used a 1,000-gallon tank of perchloroethylene ( $\text{C}_2\text{Cl}_4$ ) placed 19 feet underground. This yielded an upper bound on the rate for solar neutrino reactions of  $\sim 40,000$  SNU. Subsequent developments are described by Lande (2010). Construction began on the Homestake detector in 1965, with first results announced in 1968, and with measurements continuing until 2002, when the Homestake Mine closed. The final result

$$\langle \sigma \phi \rangle = 2.56 \pm 0.16 \pm 0.16 \text{ SNU} \quad (5)$$

is about a factor of three below historical SSM best values. (The GS98-SFII SSM rate is  $8.00 \pm 0.97$  SNU.)

The experiment exploited fortuitous properties of  $^{37}\text{Ar}$  in achieving nearly single-atom counting. The average solar neutrino reaction rate in the tank was  $0.48$  counts  $\text{day}^{-1}$ , above a background dominated by cosmogenics of  $0.09$  counts  $\text{day}^{-1}$ . As a noble gas that does not interact chemically, argon can be extracted with high efficiency ( $\gtrsim 95\%$ ) from large volumes of organic liquid. The  $^{37}\text{Ar}$  half-life of  $\sim 35$  days allowed tank concentrations to build up over a saturation time of about two months, yet also made  $^{37}\text{Ar}$  counting via EC feasible. As the decay populates the ground state of  $^{37}\text{Cl}$ , the signal is the 2.82-keV Auger electron produced as the electrons in  $^{37}\text{Cl}$  adjust to fill the K-shell vacancy. Davis developed miniaturized gas proportional counters for this counting. Taking into account detector efficiencies and losses due to  $^{37}\text{Ar}$  decaying in the tank, the number of Ar atoms counted per year was  $\sim 25$ .

The chlorine experiment was primarily sensitive to the temperature-dependent neutrino fluxes produced in the pp III and pp II cycles ( $^8\text{B} \sim 75\%$ ,  $^7\text{Be} \sim 16\%$ ). For this reason the source of the solar neutrino problem was not immediately apparent. Many candidate explanations were offered over the next 30 years, with many of these proposing changes in the SSM to produce a somewhat cooler core.

**3.1.2. Kamiokande II/III.** Confirmation of the  $^{37}\text{Cl}$  results came 21 years later from a detector originally designed for proton-decay studies. The Kamiokande I proton decay detector was upgraded in the early 1980s to Kamiokande II/III, a 3.0-kton imaging water Cherenkov detector capable of detecting solar and other low-energy neutrinos. The neutrino signal is the Cherenkov light emitted by recoiling electrons after elastic scattering (ES),  $\nu_x + e^- \rightarrow \nu'_x + e^-$ , which is sensitive to both electron and heavy-flavor neutrinos, though with the differential sensitivity  $\sigma(\nu_e)/\sigma(\nu_\mu) \sim 6$ . For incident neutrino energies  $\gg m_e c^2$ , the electron is scattered in the forward direction. Thus,

by correlating event directions with the position of the Sun, one can cut away a large background uncorrelated with solar position to reveal solar neutrino events in a forward cone.

The inner 2.14 kton of the detector was viewed by 948 20-inch Hamamatsu photomultiplier (PMT) detectors, providing  $\sim 20\%$  coverage. The innermost 0.68 kton of the detector served as the fiducial volume for solar neutrino detection. Kamiokande II operated with a  $\sim 9$ -MeV threshold, which was later reduced to 7.5 and 7.0 MeV in Kamiokande III.

The improvements made in Kamiokande II to enable solar neutrino detection included water purification to reduce low-energy backgrounds associated with radon and uranium as well as electronics upgrades to improve timing, which is vital for the reconstruction of the interaction vertices and directions of low-energy electrons and, thus, for more cleanly defining a fiducial volume for solar neutrino events. After water-sealing the cavity holding the main detector, the outer portion of the detector was instrumented with 123 PMTs to serve as a muon anticounter, and additional water was added to shield against gamma rays from the surrounding rock. Kamiokande III included improvements in the electronics, water purification system, event reconstruction and selection tools, and Monte Carlo detector simulations software.

The first production run of Kamiokande II began in January 1987. The detection of  $^8\text{B}$  solar neutrinos based on 450 days of data extending through May 1988 was announced by the Kamiokande Collab., Hirata et al. (1989). The measured flux of  $^8\text{B}$  neutrinos with energies above 9.3 MeV was found to be  $0.46 \pm 0.13$  (stat)  $\pm 0.08$  (syst) of the SSM value, confirming the deficit seen by Davis, Harmer & Hoffman (1968). Kamiokande II/III ran until February 1995, collecting 2,079 days of data. The combined analysis of all data sets yielded (Kamiokande Collab., Fukuda et al. 1996)

$$\phi(^8\text{B}) = [2.80 \pm 0.19 \text{ (stat)} \pm 0.33 \text{ (sys)}] \times 10^6 \text{ cm}^{-2} \text{ s}^{-1}, \quad (6)$$

or 50% (61%) of the GS98-SFII (AGSS09-SFII) SSM result.

The Kamiokande II/III detector was the first to record solar neutrinos event by event, establish their solar origin through correlation with the direction to the Sun, and provide direct information on the  $^8\text{B}$  spectrum through the recoil electron spectrum from ES.

**3.1.3. The gallium experiments.** Two radiochemical Ga experiments exploiting the reaction  $^{71}\text{Ga}(\nu_e, e^-)^{71}\text{Ge}$ , SAGE (Soviet–American Gallium Experiment) and GALLEX (Gallium Experiment)/GNO (Gallium Neutrino Observatory), began solar neutrino measurements in December 1989 and May 1991, respectively. SAGE, which continues to operate, uses a target of 50 tons of Ga metal, heated to  $30^\circ\text{C}$  so that the metal remains molten, and has reported results for 168 extractions through December 2007. The experiment is located in the Baksan Neutrino Observatory, under Mt. Andyrchi in the Caucasus. GALLEX, which used 30 tons of Ga in the form of a  $\text{GaCl}_3$  solution, operated through 1997, and its successor GNO continued through 2003. GALLEX and GNO were mounted in the Gran Sasso National Laboratory, near L’Aquila, Italy.

Gallium, first proposed as a solar neutrino detector by Kuzmin (1966), has a low threshold for solar neutrino absorption (233 keV) and a strong Gamow–Teller transition to the ground state of  $^{71}\text{Ge}$ . This leads to a large cross section for absorbing the low-energy pp neutrinos. As  $^{71}\text{Ge}$  has a half-life of 11.43 days, a radiochemical experiment analogous to that done for chlorine was proposed, though the chemistry of Ge recovery is considerably more complicated than that for Ar. Because of its pp neutrino sensitivity, the Ga experiment has a minimum astronomical counting rate of 79 SNU, assuming only a steady-state Sun and standard-model (SM) weak interaction physics. That is, any combination of pp I, pp II, and pp III burning consistent with the Sun’s observed luminosity leads to a solar neutrino capture rate at or above this value (Bahcall 1989).

Thus, the Ga experiment had the potential to yield a result that would require a “new physics” solution to the solar neutrino problem.

In 1974, Davis and collaborators began work on the chemistry of Ge recovery for both GaCl<sub>3</sub> solution and Ga metal, conducting a 1.3-ton pilot experiment using GaCl<sub>3</sub> in 1980–1982 to demonstrate the procedures later used by GALLEX. The method recovers Ge as GeCl<sub>4</sub> by bubbling nitrogen through the solution and then scrubbing the gas. The Ge can be further concentrated and purified, converted into GeH<sub>4</sub>, and then counted in miniaturized gas proportional counters similar to those used in the chlorine experiment.

In the SAGE experiment with room-temperature liquid metal, the <sup>71</sup>Ge is separated by mixing into the Ga a solution of hydrogen peroxide and dilute hydrochloric acid, which produces an emulsion; the Ge migrates to the surface of the emulsion as droplets, where it can be oxidized and dissolved by hydrochloric acid. The Ge is extracted as GeCl<sub>4</sub>, purified and concentrated, synthesized into GeH<sub>4</sub>, and then counted by the method described above. In both GALLEX and SAGE, the overall efficiency of the chemical procedures was determined by introducing a known amount of Ge carrier gas.

A unique aspect of the Ga experiments was the neutrino source experiments conducted to check overall experimental procedures—chemical extraction, counting, and analysis techniques. The calibrations also checked the capture cross section, as two excited-state transitions not constrained by the <sup>71</sup>Ge lifetime contribute to <sup>7</sup>Be neutrino capture. Two GALLEX calibrations and the first SAGE calibration were done with <sup>51</sup>Cr sources. A second SAGE calibration was done with a <sup>37</sup>Ar source. Source intensities were ~0.5 MCi. The weighted average (SAGE Collab., Abdurashitov et al. 2009) for the four calibrations, expressed as the ratio *R* of measured <sup>71</sup>Ge to that expected, based on calibrations of the source strengths, is  $R = 0.87 \pm 0.05 (1\sigma)$ . The discrepancy, which exceeds two standard deviations, has attracted some attention owing to other short-baseline neutrino anomalies (Abazajian et al. 2012, Gavrín et al. 2010).

The capture rate limit obtained from the first five extractions with 30 tons of Ga,  $\lesssim 79$  SNU (90% C.L.) (SAGE Collab., Abazov et al. 1991), coincided with the minimum astrophysical value. The most recent SAGE combined analysis for all 168 extractions yielded (SAGE Collab., Abdurashitov et al. 2009)

$$\langle\sigma\phi\rangle_{\text{SAGE}} = 65.4^{+3.1}_{-3.0} (\text{stat})^{+2.6}_{-2.8} (\text{syst}) \text{ SNU}, \quad (7)$$

or approximately half the unoscillated SSM best value. GALLEX announced first results in 1992, a counting rate based on 14 extractions of  $83 \pm 19 (\text{stat}) \pm 8 (\text{syst})$  SNU (GALLEX Collab., Anselmann et al. 1992). GALLEX completed four campaigns, I through IV, running until 1997. From 65 extractions and 1,594 days of data, and including updates due to new pulse-shape analysis methods, GALLEX found (GALLEX Collab., Hampel et al. 1999; Kaether et al. 2010)

$$\langle\sigma\phi\rangle_{\text{GALLEX I-IV}} = 73.1^{+6.1}_{-6.0} (\text{stat})^{+3.7}_{-4.1} (\text{syst}) \text{ SNU}. \quad (8)$$

A number of improvements in Ge extraction procedures, electronics, counter efficiency calibrations, and radon event characterization were incorporated into the follow-up experiment GNO. The experiment accumulated 1,687 days of running between May 1998 and April 2003. The counting rate from the 58 extractions is

$$\langle\sigma\phi\rangle_{\text{GNO}} = 62.9^{+5.5}_{-5.3} (\text{stat})^{+2.5}_{-2.5} (\text{syst}) \text{ SNU}. \quad (9)$$

The weighted average of SAGE, GALLEX, and GNO results is

$$\langle\sigma\phi\rangle_{\text{SAGE} + \text{GALLEX} + \text{GNO}} = 66.1 \pm 3.1 \text{ SNU}, \quad (10)$$

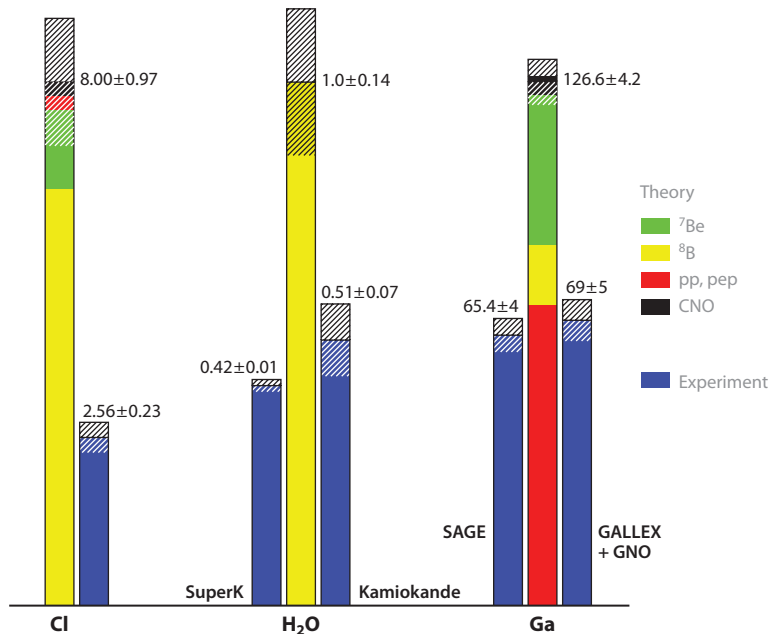


**Figure 4**

Comparison of the measured neutrino rates for the chlorine, Kamiokande II/III, and SAGE/GALLEX/GNO experiments with the contemporary GS98-SFII SSM, assuming unoscillated fluxes (Serenelli, Haxton & Peña-Garay 2011). Abbreviations: GALLEX, Gallium Experiment; GNO, Gallium Neutrino Observatory; pep, proton-electron-proton; pp, proton-proton; SAGE, Soviet-American Gallium Experiment; SuperK, Super-Kamiokande.

with all uncertainties combined in quadrature (SAGE Collab., Abdurashitov et al. 2009). The GS98-SFII SSM rate is  $126.6 \pm 4.2$  SNU.

**3.1.4. Hints of new physics.** In **Figure 4**, results of the early experiments are compared to the predictions of the contemporary GS98-SFII SSM. Not only are the results in disagreement with the SSM, but the pattern of discrepancies is not easily reproduced even if one entertains the possibility of substantial variations in that model. By the early 1990s, several analyses (Hata & Langacker 1994; Parke 1995; White, Krauss & Gates 1993) had pointed to apparent contradictions in the pattern of fluxes with respect to SSM predictions,

$$\phi(\text{pp}) \sim 0.9\phi^{\text{SSM}}(\text{pp}) \quad \phi(^7\text{Be}) \sim 0 \quad \phi(^8\text{B}) \sim 0.4\phi^{\text{SSM}}(^8\text{B}). \quad (11)$$

Variations in the SSM affect the neutrino fluxes principally through their impact on the core temperature  $T_C$ . As

$$\frac{\phi(^8\text{B})}{\phi(\text{pp})} \sim T_C^{22}, \quad (12)$$

the observation that  $\phi(^8\text{B})/\phi(\text{pp}) \sim 0.4\phi^{\text{SSM}}(^8\text{B})/\phi^{\text{SSM}}(\text{pp})$  would seem to require a cooler solar core,  $T_C \sim 0.95 T_C^{\text{SSM}}$ . However, as

$$\frac{\phi(^7\text{Be})}{\phi(^8\text{B})} \sim T_C^{-12}, \quad (13)$$

the observation that  $\phi(^7\text{Be})/\phi(^8\text{B}) \ll \phi^{\text{SSM}}(^7\text{Be})/\phi^{\text{SSM}}(^8\text{B})$  would seem to require a hotter core,  $T_C > T_C^{\text{SSM}}$ , contradicting the conclusion reached just above. Model-independent analyses assuming undistorted neutrino spectra and a steady-state Sun (so that neutrino fluxes are constrained by the Sun's luminosity) were done by Hata, Bludman & Langacker (1994) and Heeger & Robertson (1996). Their calculations showed that the probability of solutions without new particle physics was in a range of  $\sim 2\text{--}3\%$ . Heeger & Robertson (1996) further argued that if the luminosity constraint were relaxed, this probability would still be limited to  $\sim 4\%$ . The likelihood of a new-physics solution to the solar neutrino problem was high. The conclusion—that the solar neutrino problem might have its origin outside of astrophysics—was additionally supported by a growing body of evidence from helioseismology that validated SSM descriptions of the Sun's interior structure.

### 3.2. Helioseismology

Measurements and analysis of Doppler shifts of photospheric absorption lines show that the Sun's surface oscillates with amplitudes  $\sim 30$  m and velocities  $\sim 0.1$  m s<sup>-1</sup>, reflecting a variety of interior modes (Gizon & Birch 2005). Turbulence within the Sun's convective zone acts as a random driver of sound waves propagating through the gas. Specific frequencies are enhanced as standing waves, normal eigenmodes that reflect details of solar structure. Here we summarize the basics of solar oscillations, referring readers to Chaplin & Miglio (2013, in this volume) for a more detailed discussion.

The SSM is characterized by quasi-static pressure  $p(r)$ , density  $\rho(r)$ , temperature  $T(r)$ , entropy  $s(r)$ , gravitational potential  $\phi(r)$ , and nuclear energy generation  $\varepsilon(r)$  profiles that are functions of the radial coordinate  $r$ . One can perturb the SSM by introducing small displacements  $\delta\vec{r}$  and associated velocities  $v(\vec{r}) = \partial\delta\vec{r}/\partial t$  and then seek small-amplitude normal-mode solutions (Christensen-Dalsgaard 2002),

$$\rho(\vec{r}, t) \equiv \rho_0(r) + \rho'(\vec{r}, t) \quad \rho'(\vec{r}, t) \sim \rho'(r)Y_{lm}(\theta, \phi)e^{i\omega t}, \quad (14)$$

that might account for observed solar surface oscillations.

Solar oscillations can be treated in the adiabatic approximation because the timescale for heat exchange is much longer than the oscillation periods of interest. Using the adiabatic index  $\Gamma_1$  to describe the power-law dependence of the pressure on the density and the associated sound speed  $c(r)$ ,

$$\Gamma_1 \equiv \left( \frac{\partial \log p(r)}{\partial \log \rho(r)} \right)_s \quad p(r) = \frac{1}{\Gamma_1} \rho(r)c^2(r), \quad (15)$$

one can define an auxiliary field  $\Psi(\vec{r}) = c^2\sqrt{\rho(r)}\vec{\nabla} \cdot \delta\vec{r}$ . The Cowling (neglecting perturbations to the gravitational field) and adiabatic approximations (Duebner & Gough 1984) show that

$$\frac{d^2\Psi_l(r)}{dr^2} + \frac{1}{c^2} \left[ \omega^2 - \omega_{\text{co}}^2 - \frac{l(l+1)c^2}{r^2} \left( 1 - \frac{N^2}{\omega^2} \right) \right] \Psi_l(r) \equiv \left( \frac{d^2}{dr^2} + \frac{\omega_{\text{eff}}^2}{c^2} \right) \Psi_l(r) \sim 0, \quad (16)$$

where propagating (evanescent) solutions exist for  $\omega_{\text{eff}}^2 > 0$  ( $< 0$ ). This eigenvalue problem is governed by the buoyancy, or Brunt-Väisälä, frequency  $N(r)$ ,

$$N^2(r) = \frac{Gm(r)}{r} \left( \frac{1}{\Gamma_1} \frac{d \log p(r)}{dr} - \frac{d \log \rho(r)}{dr} \right), \quad (17)$$

which turns negative in the convective zone but is positive and roughly constant in the radiative interior; the Lamb frequency,

$$S_l^2(r) = \frac{l(l+1)c^2}{r^2}, \quad (18)$$

which diverges for  $r \rightarrow 0$  if  $l > 0$ ; and the acoustic cut-off frequency, which depends on the density scale height  $H(r)$  and sound speed,

$$\omega_{\text{co}}(r) = \frac{c}{2H} \sqrt{1 - 2 \frac{dH}{dr}}, \quad \text{where} \quad H(r) \equiv - \left( \frac{1}{\rho(r)} \frac{d\rho(r)}{dr} \right)^{-1}, \quad (19)$$

and determines the outer turning point where  $\omega \sim \omega_{\text{co}}$ . Eigensolutions of Equation 16 can be found for discrete frequencies  $\{\omega_{nl}\}$ , where  $n$  is the radial order: There is no dependence on  $m$  because all azimuthal modes for fixed  $n, l$  are degenerate by spherical symmetry. The assumptions leading to Equation 16 can be justified except when  $n$  and  $l$  are small or when  $l \ll n$  (Duebner & Gough 1984).

As  $\omega \gg \omega_{\text{co}}$  everywhere except near the surface, the solar regions supporting propagating solutions are determined by

$$\omega_{\text{eff}}^2 \sim \omega^2 - \frac{l(l+1)c^2}{r^2} \left( 1 - \frac{N^2}{\omega^2} \right) > 0. \quad (20)$$

Two different families of solutions exist. The g-mode family is determined by the conditions  $\omega^2 \ll N^2$  and  $\omega^2 \ll S^2$ . Consequently, g-mode propagation is confined to the solar radiative interior. The second family, the acoustic oscillations or p-modes, are the modes that have been observed in the Sun. If  $\omega^2 \gg N^2$ , then Equation 20 and the requirement  $\omega_{\text{eff}}^2 > 0$  define the inner turning-point radius

$$r_{\text{turning}} \sim \frac{c(r)}{\omega} \sqrt{l(l+1)}. \quad (21)$$

Qualitatively it is clear that the dependence of the eigenfrequencies on  $l$  can provide localized sensitivity to  $c(r)$ , with modes of low  $l$  penetrating more deeply into the solar interior. Because the eigenfrequencies depend on  $c(r)$ , the p-mode observations constrain the solar pressure and density profiles.

Similar radial sensitivity is found for the g-modes. The condition  $\omega \ll N(r)$  allows propagation in the deep interior because Equation 20 guarantees that  $\omega_{\text{eff}}^2 > 0$  for  $r$  sufficiently small. Although in principle this suggests sensitivity to  $c(r)$  in the solar core, g-modes are damped in the convective envelope, making observation difficult. No undisputed detection exists to date (Appourchaux et al. 2010).

The significant effort invested in helioseismological measurements and analysis has yielded a rather precise map of  $c(r)$  over the outer 90% of the Sun by radius. The solar profile used in **Figure 5** was obtained by Basu et al. (2009) from an analysis that included 4,752 days of BiSON data (<http://bison.ph.bham.ac.uk>). The comparison SSMs are AGSS09-SFII [ $(Z/X)_S = 0.0178$ ] and GS98-SFII [ $(Z/X)_S = 0.0229$ ].

GS98-SFII is representative of models that were in use in the 1990s: The generally good agreement with the solar  $c(r)$  ( $\sim 0.2\%$  apart from a narrow region just below the convective boundary) was taken as strong support for the SSM, helping to reinforce the conclusion that the solar neutrino problem might have a particle physics origin. Helioseismic data forced improvements in the SSM, such as the inclusion of helium and heavy-element diffusion (Bahcall & Pinnsoneault 1992, 1995). The suggestion from early solar neutrino experiments and helioseismology that new particle physics could be the source of the solar neutrino problem provided additional motivation for a new generation of sophisticated experiments with high statistics and sensitivity to neutrino flavor, spectral distortions, and day-night differences, described below.

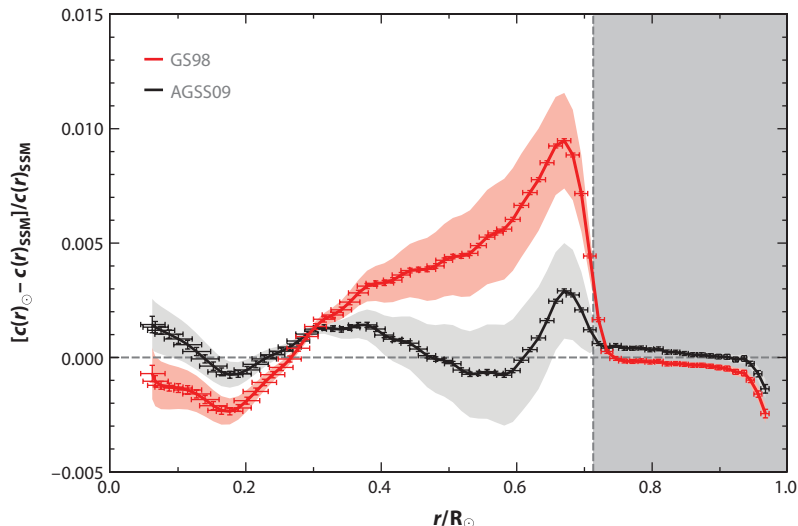


**Figure 5**

The relative sound speed  $[c(r)_\odot - c(r)_{\text{SSM}}]/c(r)_{\text{SSM}}$ , where  $c(r)_{\text{SSM}}$  is the standard solar model (SSM) result and  $c(r)_\odot$  the solar profile extracted from BiSON data (error bars indicated). The black and red profiles correspond to the high-metallicity GS98-SFII and low-metallicity AGSS09-SFII SSMs, respectively. The bands are 1-sigma contours from solar modeling, including the quadrature influences of elemental abundances, cross sections, and diffusion rates, but with correlations neglected.

### 3.3. Super-Kamiokande

Super-Kamiokande, the successor to the Kamiokande detector, is a 50-kton cylindrical water Cherenkov detector located in the Kamioka Mine at an effective depth of  $\sim 2.03$  km of water equivalent (km.w.e). The inner 32 kton of water is viewed by  $\sim 11,100$  20-inch PMTs (40% coverage), with 22.5 kton serving as the fiducial volume for detecting solar neutrinos. The detector has operated at (total) electron energy thresholds for solar neutrinos ranging from 7.0 to the present 4.0 MeV, so that detection is limited to  $^8\text{B}$  and hep neutrinos. Although in ES the energy of the incident neutrino is shared between the scattered electron and outgoing neutrino, electron detection provides some sensitivity to the initial neutrino spectrum and, thus, to distortions associated with neutrino oscillations (Super-Kamiokande Collab. 2012; Super-Kamiokande Collab., S. Fukuda et al. 2003). The electron energy resolution at 10 MeV is  $\sim 16\%$ .

The detector began operations in 1996, progressing from phase I to the current phase IV. Super-Kamiokande I recorded neutrino events for approximately five years, determining an  $^8\text{B}$  neutrino flux of  $\phi(^8\text{B}) = [2.35 \pm 0.02 (\text{stat}) \pm 0.08 (\text{syst})] \times 10^6 \text{ cm}^{-2} \text{ s}^{-1}$  from events recorded above 5 MeV, assuming an undistorted spectrum (Super-Kamiokande Collab., Hosaka et al. 2006). The measured rate variation of  $\sim 7\%$  over the year is consistent in magnitude and phase with the effects of Earth's orbital eccentricity, 1.7%. No evidence was found for spectral distortions or day-night differences, two signatures of neutrino oscillations in matter.

The detector was drained following phase I for repairs and maintenance. During refilling, the implosion of a phototube led to a chain reaction of failures that destroyed most of the lower part of the detector. Super-Kamiokande II was subsequently rebuilt with the remaining phototubes enclosed in acrylic shields. Despite the reduced phototube coverage of 19% and resulting higher threshold of 7 MeV, Super-Kamiokande II ran successfully as a solar neutrino detector

for three years, beginning in late 2002. The deduced rate,  $\phi(^8\text{B}) = [2.38 \pm 0.05 \text{ (stat)}_{-0.15}^{+0.16} \text{ (sys)}] \times 10^6 \text{ cm}^{-2} \text{ s}^{-1}$ , is consistent with Super-Kamiokande I results. No spectral distortion was detected, and the day-night difference was again consistent with zero at  $1\sigma$  (Super-Kamiokande Collab., Cravens et al. 2008).

Super-Kamiokande III (Super-Kamiokande Collab., Abe et al. 2011) collected nearly two years of data between October 2006 and August 2008, operating with a fully restored set of 11,129 PMTs equipped with shields, providing 40% phototube coverage. Improvements made to the water purification system, event reconstruction and selection tools, and the Monte Carlo detector simulation software resulted in a reduced systematic uncertainty of  $\pm 2.1\%$ . The observed event rate for electrons between 5.0 and 20 MeV is equivalent to an unoscillated  $^8\text{B}$  neutrino flux of  $2.39 \pm 0.04 \text{ (stat)} \pm 0.05 \text{ (sys)} \times 10^6 \text{ cm}^{-2} \text{ s}^{-1}$  (Super-Kamiokande Collab., Smy et al. 2013). No significant spectral distortion was observed.

Preliminary results from 1,069 days of running for Super-Kamiokande IV were reported at Neutrino 2012 (the XXV International Conference on Neutrino Physics and Astrophysics held in Kyoto, Japan, June 3–9, 2012) (Super-Kamiokande Collab., Smy et al. 2013). This latest phase of Super-Kamiokande includes new electronics, an improved Monte Carlo model of the trigger efficiency, higher efficiency due to relaxed cuts against radioactivity backgrounds, and a lower threshold of 4 MeV (total energy).

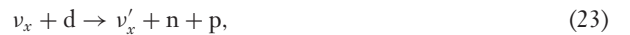
### 3.4. Sudbury Neutrino Observatory

Chen (1985) pointed out the merits of deuterium for solar neutrino detection and, five years later, construction began on the SNO two kilometers below ground, within the INCO Creighton nickel mine, Ontario, Canada (Jelley, McDonald & Robertson 2009). A kiloton of heavy water was contained in a 12-m diameter spherical acrylic vessel. A surrounding array of 9,500 20-cm PMTs viewed the inner volume, providing  $\sim 56\%$  coverage; 7 kton of light water provided a 5-m buffer between the central detector and the surrounding rock walls.

Chen recognized the advantages of the multiple detection channels that could be introduced by replacing the hydrogen in an ordinary water Cherenkov detector with deuterium. The flux of higher energy solar electron neutrinos can be probed with the CC reaction,



by detecting the produced electron. As the Gamow-Teller strength is concentrated near the 1.44-MeV breakup threshold for deuterium, the electrons carry off most of the energy and thus provide significant information on the incident neutrino spectrum. A second channel, the NC reaction



is independent of the neutrino flavor  $x$ , counting all neutrinos above the 2.22-MeV breakup threshold. As the only detectable signal of the reaction is the produced neutron, this channel placed very stringent constraints on the radioactive cleanliness of the detector. The third channel is the ES reaction of conventional water detectors,



Operations were carried out in three phases. SNO I operated with pure heavy water. The NC-channel neutrons can capture on deuterium, producing 6.25-MeV gamma rays that Compton scatter off electrons, producing light for recoils above the Cherenkov threshold. SNO I operations covered 306.4 live days from November 1999 through May 2001. Two analyses were performed based on the assumption of an undistorted  $^8\text{B}$  spectrum using electron kinetic energy thresholds of 6.75 and 5 MeV, respectively. The second analysis thus included NC events.

In SNO II, two tons of purified NaCl were dissolved in the water, so that  $^{35}\text{Cl}(n, \gamma)$  would become the dominant neutron sink. This reaction increases the capture rate and energy release. Data were accumulated for 391.4 live days from July 2001 through August 2003. Detector calibrations completed in SNO I were repeated and extended in SNO II, including new checks involving the introduction of beta-gamma sources that could lead to photo-disintegration of deuterium and the use of a  $^{252}\text{Cf}$  neutron source to determine the neutron detection efficiency. The analysis was performed for a kinetic energy threshold of 5.5 MeV and treated the first 254.2 live days of data as blind. In addition, the  $^8\text{B}$  spectrum shape was not assumed, but rather extracted from the analysis, using 0.5-MeV bins from 5.5 to 13.5 MeV, plus an additional bin for events between 13.5 and 20 MeV.

In the first two phases of SNO the CC, ES, and NC rates were determined by a statistical analysis that decomposed the common signal, the Cherenkov light, into the three contributing components. The analysis exploited distinguishing angular correlations with respect to the Sun and energy differences in the CC-, ES-, and NC-associated light. In SNO III, the separation of the NC and CC/ES signals was accomplished by direct counting of NC neutrons. The salt introduced in SNO II was removed by reverse osmosis and ion exchange, and a month of data was taken to confirm that the detector had been restored to the operating conditions of SNO I. Then an array of the specially designed  $^3\text{He}$ - and  $\text{CF}_4$ -filled gas proportional counters was installed for neutron detection by  $^3\text{He}(n,p)^3\text{H}$ . This neutral-current detection (NCD) array consisted of 40 strings of proportional counters, ranging in length from 9 to 11 meters, that were anchored to the inner surface of the acrylic vessel, forming a lattice on a 1-m grid.

Between November 2004 and November 2006, 385.17 live days of SNO III data were taken. Extensive calibrations of both the NCD and PMT arrays were made, utilizing various neutron and gamma-ray sources, in order to calibrate the effectiveness of the neutron detection and the impact of array installation on detector behavior. The array was exploited to characterize neutron backgrounds within the detector, including the distribution and isotopic composition of background sources. During solar neutrino running, data were culled to eliminate strings that exhibited mechanical or electrical faults or to eliminate runs (operational periods of at least 30 min) when any array abnormalities were observed. A blind analysis of the remaining data was then performed. The neutrino spectrum was again determined from the CC and ES data, not assumed.

The SNO I/II and SNO III results are in generally good agreement, and both separately and in combination established the following:

1. A total flux of active neutrinos from  $^8\text{B}$  decay of  $\phi_{\text{NC}}(\nu_{\text{active}}) = [5.25 \pm 0.16 \text{ (stat)}_{-0.13}^{+0.11} \text{ (syst)}] \times 10^6 \text{ cm}^{-2} \text{ s}^{-1}$ , in good agreement with SSM predictions, and  $\phi_{\text{CC}}(\nu_e) \sim 0.34 \phi_{\text{NC}}(\nu_{\text{active}})$ ; and
2. The absence of statistically significant day-night effects or spectral distortions in the portion of the  $^8\text{B}$  neutrino spectrum above  $\sim 5$  MeV.

### 3.5. Borexino

The Borexino experiment (Borexino Collab., Alimonti et al. 2009), located in the Gran Sasso Laboratory at an effective depth of about 3.0 km.w.e., is the first to measure low-energy ( $< 1$  MeV) solar neutrino events in real time. The detector is housed within a 16.9-m domed tank containing an outer layer of ultrapure water that provides shielding against external neutrons and gamma rays. At the inner edge of the water a stainless steel sphere serves as a support structure for an array of PMT tubes that view both the inner detector and the outer water shield, so that the Cherenkov light emitted by muons passing through the water can be used to veto those events. Within the steel sphere there are two regions, separated by thin nylon vessels, containing high-purity buffer liquid, within which is sequestered a central volume of 278 tons of organic scintillator. The fiducial

volume consists of  $\sim 100$  tons of the liquid scintillator at the very center of the detector. Scintillation light produced by recoil electrons after ES events is the solar neutrino signal. The 862-keV  ${}^7\text{Be}$  neutrinos produce a recoil electron spectrum with a distinctive cut-off edge at 665 keV.

The Borexino Collaboration reported the following results in 2008 and 2011 constraining the fluxes of three low-energy solar neutrino branches (Borexino Collab., Bellini et al. 2011, 2012a):

1. A  ${}^7\text{Be}$  solar rate equivalent to an unoscillated flux of  $(3.10 \pm 0.15) \times 10^9 \text{ cm}^{-2} \text{ s}^{-1}$  or about 62% of the GS98-SFII SSM central value;
2. An ES rate for  ${}^8\text{B}$  neutrinos, based on an integration above 3 MeV, corresponding to an equivalent flux of  $\phi^{\text{ES}}({}^8\text{B}) = (2.4 \pm 0.4 \pm 0.1) \times 10^6 \text{ cm}^{-2} \text{ s}^{-1}$  (Borexino Collab., Bellini et al. 2010), which is less precise than, but in good agreement with, SNO and Super-Kamiokande results. [A similar result has been obtained by the KamLAND Collaboration,  $\phi^{\text{ES}}({}^8\text{B}) = (2.77 \pm 0.26 \pm 0.32) \times 10^6 \text{ cm}^{-2} \text{ s}^{-1}$  from events above their 5.5 MeV analysis threshold (KamLAND Collab., Abe et al. 2011).];
3. The first direct, exclusive determination of the pep flux,  $(1.6 \pm 0.3) \times 10^8 \text{ cm}^{-2} \text{ s}^{-1}$  (95% C.L.); and
4. A limit on the CNO neutrino flux,  $\phi_{\text{CNO}} < 7.7 \times 10^8 \text{ cm}^{-2} \text{ s}^{-1}$  at 95% C.L.

The Borexino  ${}^7\text{Be}$  measurement places an important constraint on matter effects in neutrino oscillations, as this line lies in a region dominated by vacuum oscillations, whereas the Super-Kamiokande and SNO measurements are done in the matter-dominated region.

#### 4. NEW NEUTRINO PROPERTIES

The results just described have been addressed in global analyses that extract from the experiments constraints on neutrino and solar properties. Before describing such analyses, we discuss some of the associated weak interactions issues. As previously noted, Kamiokande II/III had finished operations by 1994, confirming the neutrino deficit that Davis, Harmer, and Hoffman had first discovered 26 years earlier, and the SAGE and GALLEX experiments had converged on a counting rate very close to the minimum astrophysical value of 78 SNU. The pattern of pp,  ${}^7\text{Be}$ , and  ${}^8\text{B}$  fluxes that emerged from analyses of the three early experiments (see Equation 11) was inconsistent with possible SSM variations altering  $T_{\text{C}}$  [see figures by Castellani et al. (1994) and Hata, Bludman & Langacker (1994) included in Haxton (1995)] and improbable in model-independent analyses that assumed only undistorted spectra of electron neutrinos (Hata, Bludman & Langacker 1994; Heeger & Robertson 1996). The agreement between the SSM sound speed profile and that deduced from helioseismology also made it more difficult to motivate SSM changes.

A variety of new particle-physics solutions to the solar neutrino problem has been suggested over the years, including vacuum and matter-enhanced neutrino oscillations, neutrino decay (Bahcall, Cabibbo & Yahil 1972), and weakly interacting massive particles that might be bound in the Sun and consequently contribute to energy transport (Faulkner & Gilliland 1985, Spergel & Press 1985). In addition to the standard MSW scenario, other oscillation effects in matter were explored, including spin-flavor resonances driven by neutrino magnetic moments (Akhmedov 1988, Lim & Marciano 1988), parametric density fluctuations (Schafer & Koonin 1987, Krastev & Smirnov 1989), contributions to the MSW potential from currents (Haxton & Zhang 1991), and depolarization in the stochastic fluctuation limit (Loreti & Balantekin 1994).

Of these and other possibilities, the MSW mechanism drew the most attention because of its minimal requirements, neutrino masses, and a vacuum mixing angle  $\theta_{\nu} \gtrsim 10^{-4}$ . Although neutrinos are massless in the SM, and consequently cannot oscillate, nonzero masses arise in most extensions of the model. Small weak-interaction mixing angles were already familiar from the analogous quark mixing matrix.

#### 4.1. Oscillation Basics: The Vacuum Case

The current laboratory (tritium  $\beta$  decay) limit on the  $\bar{\nu}_e$  mass is 2.3 eV, though an effort is underway to substantially improve this bound (KATRIN Collab., Angrik et al. 2004; Otten & Weinheimer 2008). Cosmological analyses variously limit the sum over mass eigenstates to  $\sum_i m_\nu(i) \lesssim 0.2\text{--}0.6$  eV (Abazajian et al. 2011).

Two types of neutrino mass terms can be added to the SM. Neutrinos can have Dirac masses, analogous to those of other SM fermions, if the SM is enlarged to include a right-handed neutrino field. Because neutrinos lack charges or other additively conserved quantum numbers, lepton-number-violating Majorana mass terms can also be added,  $\bar{\nu}_L^c m_L \nu_L$  and  $\bar{\nu}_R^c m_R \nu_R$ , where the former is the only dimension-five operator that can be constructed in the SM. (The subscripts L and R denote left- and right-hand projections of the neutrino field  $\nu$ , and the superscript  $c$  denotes charge conjugation.)

In the seesaw mechanism (Gell-Mann, Ramond & Slansky 1979; Mohapatra & Senjanovic 1980; Schechter & Valle 1980, 1982; Yanagida 1980), the Dirac and Majorana mass terms are combined in a manner that provides an attractive explanation for light neutrinos,

$$M_\nu \sim \begin{pmatrix} 0 & m_D \\ m_D^T & m_R \end{pmatrix},$$

where  $m_L \sim 0$  in part because of double beta decay constraints. When diagonalized, the matrix yields heavy and light neutrino mass eigenstates,

$$m_H \sim m_R \quad m_L \sim m_D \frac{m_D}{m_R},$$

with the latter related to the typical Dirac mass of the SM by the coefficient  $m_D/m_R$ . If we assume the scale of the new physics that  $m_R$  represents is  $\gg m_D$ , then a candidate small parameter  $m_D/m_R$  is available to explain why neutrinos are so much lighter than other SM fermions. Small neutrino masses are thus explained as a consequence of the scale  $m_R$  of new physics beyond the SM.

Neutrinos of definite mass are the eigenstates for free propagation, whereas neutrino flavor eigenstates are produced in weak interactions. Simplifying here to two flavors, the relationship of the flavor  $\{\nu_e, \nu_\mu\}$  and mass  $\{\nu_1, \nu_2\}$  eigenstates can be described by a single vacuum mixing angle  $\theta_V$ ,

$$\nu_e = \cos \theta_V |\nu_1\rangle + \sin \theta_V |\nu_2\rangle \quad \nu_\mu = -\sin \theta_V |\nu_1\rangle + \cos \theta_V |\nu_2\rangle. \quad (25)$$

Consequently, an arbitrary initial state  $|\nu(t=0)\rangle = a_e(t=0)|\nu_e\rangle + a_\mu(t=0)|\nu_\mu\rangle$  of momentum  $k \sim E$ , as it propagates downstream, evolves according to

$$i \frac{d}{dt} \begin{pmatrix} a_e \\ a_\mu \end{pmatrix} = \frac{1}{4E} \begin{pmatrix} -\delta m_{21}^2 \cos 2\theta_V & \delta m_{21}^2 \sin 2\theta_V \\ \delta m_{21}^2 \sin 2\theta_V & \delta m_{21}^2 \cos 2\theta_V \end{pmatrix} \begin{pmatrix} a_e \\ a_\mu \end{pmatrix}, \quad (26)$$

where an average overall wave function phase has been removed from the neutrino mass matrix (represented in the flavor basis). For the special case of a  $\nu_e$  produced at time  $t = 0$ , the solution of this equation yields

$$P_{\nu_e}(t) = |\langle \nu_e | \nu(t) \rangle|^2 = 1 - \sin^2 2\theta_V \sin^2 \left( \frac{\delta m_{21}^2 t}{4E} \right) \rightarrow 1 - \frac{1}{2} \sin^2 2\theta_V, \quad (27)$$

where the downstream oscillation depends on the difference  $\delta m_{21}^2 \equiv m_2^2 - m_1^2$ . (If this problem is properly studied with wave packets, the oscillation persists until the two mass components separate spatially, yielding the asymptotic result on the right.) The oscillation length  $L_0 = 4\pi \hbar c E / \delta m_{21}^2 c^4$

is shorter than the Earth-Sun distance for a typical solar neutrino of energy  $\sim 1$  MeV provided  $\delta m_{21}^2 \gtrsim 1.6 \times 10^{-11} \text{ eV}^2$ . Thus, solar neutrinos are interesting for oscillation studies because of their sensitivity to extremely small neutrino mass differences.

## 4.2. Oscillation Basics: Matter and the Mikheyev-Smirnov-Wolfenstein Mechanism

Mikheyev & Smirnov (1985, 1986) showed that the density dependence of the neutrino effective mass, a phenomenon first discussed by Wolfenstein (1978a,b), could greatly enhance oscillation probabilities. Their original numerical work was soon understood analytically as a consequence of level crossing: a neutrino produced in the core as a  $\nu_e$  is adiabatically transformed into a  $\nu_\mu$  by traversing a critical solar density where the  $\nu_e$  and  $\nu_\mu$  effective masses cross. It became clear that the Sun is not only an excellent neutrino source but also a natural regenerator for enhancing the effects of flavor mixing.

Equation 26 describing vacuum oscillations is altered in matter,

$$i \frac{d}{dx} \begin{pmatrix} a_e \\ a_\mu \end{pmatrix} = \frac{1}{4E} \begin{pmatrix} 2E\sqrt{2}G_F\rho(x) - \delta m_{21}^2 \cos 2\theta_V & \delta m_{21}^2 \sin 2\theta_V \\ \delta m_{21}^2 \sin 2\theta_V & -2E\sqrt{2}G_F\rho(x) + \delta m_{21}^2 \cos 2\theta_V \end{pmatrix} \begin{pmatrix} a_e \\ a_\mu \end{pmatrix}, \quad (28)$$

where  $G_F$  is the weak coupling constant and  $\rho(x)$  the solar electron number density. The new contribution to the difference in diagonal elements,  $4E\sqrt{2}G_F\rho(x)$ , represents the effective contribution to  $m_\nu^2$  that arises from neutrino-electron scattering. The indices of refraction of electron and muon neutrinos differ because the former scatter via charged currents and NCs, whereas the latter have only NC interactions. For  $\theta_V \lesssim \pi/4$ —the “normal hierarchy” where the lighter mass eigenstate makes the larger contribution to  $\nu_e$  in vacuum—the matter and vacuum contributions to the diagonal elements of Equation 28 have opposite signs.

We can diagonalize the right-hand side of Equation 28 to determine the heavy and light local mass eigenstates and eigenvalues  $m_H(x)$  and  $m_L(x)$ , functions of  $\rho(x)$ :

$$|\nu_L(x)\rangle = \cos\theta(x)|\nu_e\rangle - \sin\theta(x)|\nu_\mu\rangle \quad |\nu_H(x)\rangle = \sin\theta(x)|\nu_e\rangle + \cos\theta(x)|\nu_\mu\rangle, \quad (29)$$

where the local mixing angle

$$\sin 2\theta(x) = \frac{\sin 2\theta_V}{\sqrt{X^2(x) + \sin^2 2\theta_V}} \quad \cos 2\theta(x) = \frac{-X(x)}{\sqrt{X^2(x) + \sin^2 2\theta_V}} \quad (30)$$

depends on  $X(x) = 2\sqrt{2}G_F\rho(x)E/\delta m_{21}^2 - \cos 2\theta_V$ . Unlike the vacuum case, these are eigenstates for propagation only if  $\rho(x)$  is constant. Otherwise, defining  $|\nu(x)\rangle = a_H(x)|\nu_H(x)\rangle + a_L(x)|\nu_L(x)\rangle$ , Equation 28 becomes

$$i \frac{d}{dx} \begin{pmatrix} a_H \\ a_L \end{pmatrix} = \frac{1}{4E} \begin{pmatrix} \lambda(x) & i\alpha(x) \\ -i\alpha(x) & -\lambda(x) \end{pmatrix} \begin{pmatrix} a_H \\ a_L \end{pmatrix}. \quad (31)$$

The splitting of the local mass eigenstates and the local oscillation length are

$$\lambda(x) = \delta m_{21}^2 \sqrt{X^2(x) + \sin^2 2\theta_V} \quad L_0(x) = \frac{4\pi \hbar c E}{\lambda(x)c^4}, \quad (32)$$

whereas eigenstate mixing is governed by the density gradient,

$$\alpha(x) = \left( \frac{4E^2}{\delta m_{21}^2} \right) \frac{\sqrt{2} G_F \frac{d}{dx} \rho(x) \sin 2\theta_V}{X^2(x) + \sin^2 2\theta_V}. \quad (33)$$

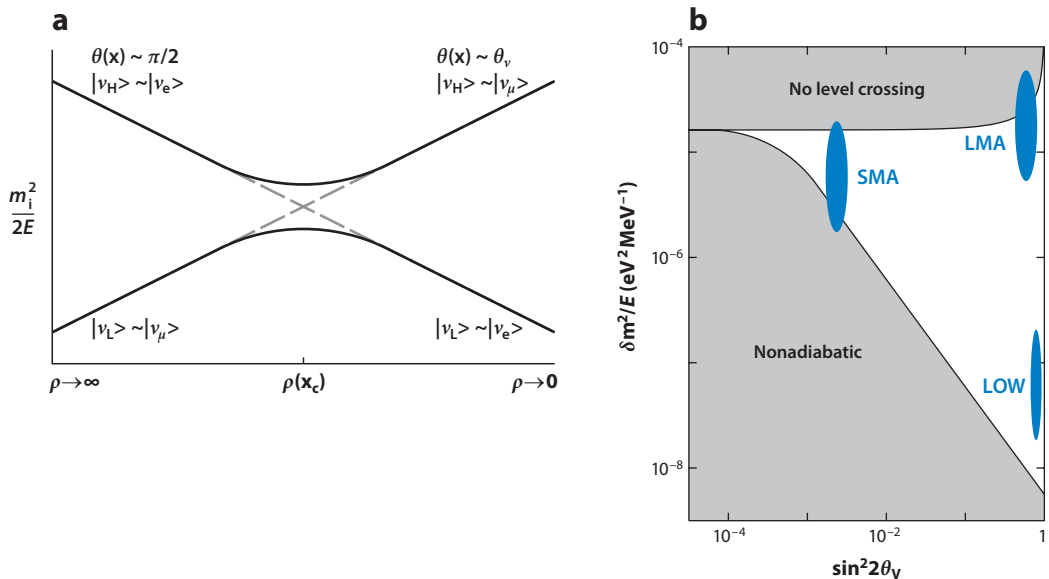


**Figure 6**

(a) A schematic illustration of the Mikheyev-Smirnov-Wolfenstein (MSW) crossing for a normal hierarchy and small  $\theta_V$ . The dashed lines—the electron-electron and muon-muon diagonal elements of the  $m_i^2$  matrix—intersect at the level-crossing density  $\rho_c$ . The solid lines are the trajectories of the light and heavy local mass eigenstates. A  $\nu_e$  produced at high density as  $\sim \nu_H$  will, under adiabatic propagation, remain  $\sim \nu_H$ , exiting the Sun as  $\sim \nu_\mu$ . (b) The white “MSW triangle” is the region where a level crossing occurs and propagation is adiabatic, producing strong  $\nu_e \rightarrow \nu_\mu$  conversion. Regions of three possible MSW solutions frequently discussed in the 1990s are depicted by the blue ellipses. Abbreviations: LMA, large mixing angle; LOW, low probability and low mass; SMA, small mixing angle.

The splitting achieves its minimum value,  $2\delta m_{21}^2 \sin 2\theta_V$ , at a critical density  $\rho_c = \rho(x_c)$  where  $X(x) \rightarrow 0$ ,

$$2\sqrt{2}EG_F\rho_c = \delta m_{21}^2 \cos 2\theta_V. \quad (34)$$

The diagonal elements of the original flavor matrix of Equation 28 cross at  $\rho_c$ .

The crux of the MSW mechanism is the adiabatic crossing of the critical density, illustrated in **Figure 6a**. The adiabatic condition is determined by the requirement  $\gamma(x) = \left| \frac{\lambda(x)}{\alpha(x)} \right| \gg 1$ , which allows one to treat Equation 31 as diagonal. This condition becomes particularly stringent near the crossing point,

$$\gamma_c \equiv \gamma(x_c) = \frac{\sin^2 2\theta_V}{\cos 2\theta_V} \frac{\delta m_{21}^2}{2E} \frac{1}{\left| \frac{1}{\rho_c} \frac{d\rho(x)}{dx} \right|_{x=x_c}} = 2\pi \tan 2\theta_V \frac{H_c}{L_c} \gg 1, \quad (35)$$

where  $H_c$  and  $L_c$  are the solar density scale height and local oscillation length at  $x_c$ . If the  $H_c \gg L_c$ , Equation 31 then yields (Bethe 1986)

$$P_{\nu_e}^{\text{adiab}} = \frac{1}{2} + \frac{1}{2} \cos 2\theta_V \cos 2\theta_i, \quad (36)$$

where  $\theta_i = \theta(x_i)$  is the local mixing angle at the density where the neutrino is produced. The adiabatic solution depends on the local mixing angles where the neutrino begins ( $\theta_i$ , solar core) and ends ( $\theta_V$ , in vacuum) its propagation.

For illustration, consider the case of a small  $\theta_V \sim 0$ . A solar  $\nu_e$  created in the high-density solar core is then nearly identical to the heavy-mass eigenstate ( $\theta_i \sim \pi/2$ ), provided the vacuum mass difference between the eigenstates is not too large (see Equation 30). If the subsequent propagation is adiabatic, the neutrino remains on the heavy-mass trajectory, crossing the critical density [ $\theta(x_c) = \pi/4$ ], and finally exiting the Sun. But in vacuum, the heavy-mass eigenstate is  $\sim \nu_\mu$ : A nearly complete flavor change,  $\nu_e \rightarrow \nu_\mu$ , has occurred through an adiabatic rotation of the local oscillation angle from  $\theta_i \sim \pi/2$  to  $\theta_f = \theta_V$  during propagation.

If the adiabatic condition is not satisfied, e.g.,  $\gamma_c \lesssim 1$ , an accurate analytic solution can still be obtained (Haxton 1986, Parke 1986). As we have seen, the nonadiabatic behavior is governed by the density scale height at  $x_c$ . One can replace the actual solar density by an effective one, e.g., a linear density “wedge” that has the correct derivative at  $x_c$  (thereby incorporating the effects of the density gradient at the most sensitive point), while also starting and ending at the appropriate initial and final densities (thereby also building in the adiabatic limit). The resulting generalization of Equation 36 is

$$P_{\nu_e} = \frac{1}{2} + \frac{1}{2} \cos 2\theta_V \cos 2\theta_i (1 - 2P_{\text{hop}}) \quad P_{\text{hop}} \equiv e^{-\pi\gamma_c/2}, \quad (37)$$

where  $P_{\text{hop}}$ , the Landau-Zener probability of hopping from the heavy-mass trajectory to the light trajectory on traversing  $x_c$ , vanishes in the highly adiabatic limit,  $\gamma_c \gg 1$  (so that Equation 37 reduces to Equation 36). When the crossing becomes highly nonadiabatic ( $\gamma_c \ll 1$ ), then  $P_{\text{hop}} \rightarrow 1$ : The neutrino exits the Sun on the light mass trajectory, which for small mixing angles (SMAs) means it remains  $\sim \nu_e$ .

Thus, strong conversion of solar neutrinos is expected when (a) the propagation is adiabatic ( $\gamma_c \gtrsim 1$ ) and (b) there is a level crossing [there is enough matter at the  $\nu_e$  production point that  $\nu_e(x_i) \sim \nu_H(x_i)$ ]. **Figure 6b** shows the white triangle of parameters in the  $\delta m_{21}^2/E - \sin^2 2\theta_V$  plane, where both constraints are satisfied. Within this triangle, strong conversion occurs. One can envision superimposing on this triangle the spectrum of solar neutrinos, plotted as a function of  $\delta m_{21}^2/E$  for some choice of  $\delta m_{21}^2$  and  $\theta_V$ . Depending on how that spectrum is positioned vertically (a function of  $\delta m_{21}^2$ ) or horizontally (a function of  $\theta_V$ ), the resulting spectrum of  $\nu_e$ s can be altered in several characteristic ways, for example, suppressing the low-energy or high-energy neutrinos preferentially, or even (in the case of SMAs) those of intermediate energy.

In early fits to the neutrino data, three potential MSW solutions were frequently discussed, designated by SMA (small mixing angle;  $\delta m_{21}^2 \sim 5.4 \times 10^{-6}$  eV,  $\sin^2 2\theta_V \sim 0.006$ ), LMA (large mixing angle;  $\delta m_{21}^2 \sim 1.8 \times 10^{-5}$  eV,  $\sin^2 2\theta_V \sim 0.76$ ), and LOW (low probability, low mass;  $\delta m_{21}^2 \sim 7.9 \times 10^{-8}$  eV,  $\sin^2 2\theta_V \sim 0.96$ ). (The parameter values are taken from Bahcall, Krastev & Smirnov (1998) and are representative of fits done at that time.) These solutions are indicated schematically by the colored regions in **Figure 6**. As was shown by the KamLAND experiment (Eguchi et al. 2003), the solution consistent with the solar neutrino data proved, ironically, to be the LMA solution—not the SMA solution where matter effects so greatly enhance the oscillations.

## 5. GLOBAL ANALYSES AND NEUTRINO PROPERTIES

Neutrino physics has made great progress in the past 15 years as reactor and accelerator neutrino experiments have added new information to that obtained from solar and atmospheric neutrino experiments. The three mixing angles of the  $3 \times 3$  neutrino mass matrix, the magnitudes of the two mass differences, and (from solar neutrino experiments) the sign of one of these mass differences have all been determined. The phenomena that can be explored with solar neutrinos were illustrated previously for the two-flavor case: Flavor oscillations, affected by matter, not only alter fluxes but lead to distinctive spectral distortions and may produce day-night differences

owing to neutrino passage through Earth. The various experimental collaborations as well as independent groups have developed global analysis methods to analyze solar neutrino experiments, taking into account the constraints other recent measurements have imposed. Here, we summarize the conclusions of such analyses, relying particularly on work done by the Bari and Valencia groups.

### 5.1. Vacuum Mixing Angles and Mass<sup>2</sup> Differences

In the SM case of three light neutrino flavors, the relationship between flavor  $\{\nu_e, \nu_\mu, \nu_\tau\}$  and mass  $\{\nu_1, \nu_2, \nu_3\}$  eigenstates is described by the PMNS matrix (Maki, Nakagawa & Sakata 1962; Pontecorvo 1967),

$$\begin{pmatrix} |\nu_e\rangle \\ |\nu_\mu\rangle \\ |\nu_\tau\rangle \end{pmatrix} = \begin{pmatrix} c_{12}c_{13} & s_{12}c_{13} & s_{13}e^{-i\delta} \\ -s_{12}c_{23} - c_{12}s_{23}s_{13}e^{i\delta} & c_{12}c_{23} - s_{12}s_{23}s_{13}e^{i\delta} & s_{23}c_{13} \\ s_{12}s_{23} - c_{12}c_{23}s_{13}e^{i\delta} & -c_{12}s_{23} - s_{12}c_{23}s_{13}e^{i\delta} & c_{23}c_{13} \end{pmatrix} \begin{pmatrix} e^{i\alpha_1/2}|\nu_1\rangle \\ e^{i\alpha_2/2}|\nu_2\rangle \\ |\nu_3\rangle \end{pmatrix}, \quad (38)$$

where  $c_{ij} \equiv \cos \theta_{ij}$  and  $s_{ij} \equiv \sin \theta_{ij}$ . This matrix depends on three mixing angles  $\theta_{12}$ ,  $\theta_{13}$ , and  $\theta_{23}$ , of which the first and last are the dominant angles for solar and atmospheric oscillations, respectively; a Dirac phase  $\delta$  that can induce charge parity-violating differences in the oscillation probabilities for conjugate channels such as  $\nu_\mu \rightarrow \nu_e$  versus  $\bar{\nu}_\mu \rightarrow \bar{\nu}_e$ ; and two Majorana phases  $\alpha_1$  and  $\alpha_2$  that will affect the interference among mass eigenstates in the effective neutrino mass probed in the lepton-number-violating process of neutrinoless double  $\beta$  decay.

It became apparent, in early analyses that combined solar and reactor neutrino data in two-flavor analyses, that there was some hint of the third flavor, a nonzero  $\theta_{13}$ . The KamLAND Collaboration analysis employed the three-flavor  $\nu_e$  survival probability of Fogli et al. (2000) in which the influence of  $\theta_{13}$  in modifying the two-flavor result is explicit:

$$P_{ee}^{3\nu} = \cos^4 \theta_{13} \bar{P}_{ee}^{2\nu} + \sin^4 \theta_{13}, \quad (39)$$

where  $\bar{P}_{ee}^{2\nu}$  is the two-flavor survival probability in matter evaluated for the modified electron density  $\rho(x) \rightarrow \rho(x) \cos^2 \theta_{13}$ . The analysis yielded  $\sin^2 \theta_{13} = 0.020 \pm 0.016$  (KamLAND Collab., Gando et al. 2011), a result consistent with the long-baseline  $\nu_e$  appearance results announced shortly afterward,  $0.008 \lesssim \sin^2 \theta_{13} \lesssim 0.094$  (T2K Collab., K. Abe et al. 2011) and  $0.003 \lesssim \sin^2 \theta_{13} \lesssim 0.038$  (MINOS Collab., Adamson et al. 2011). In 2012, results from reactor  $\bar{\nu}_e$  disappearance experiments became available, yielding  $\sin^2 \theta_{13} = 0.022 \pm 0.011$  (stat)  $\pm 0.008$  (sys) (Double Chooz Collab., Abe et al. 2012),  $\sin^2 \theta_{13} = 0.0236 \pm 0.0042$  (stat)  $\pm 0.0013$  (sys) (Daya Bay Collab., An et al. 2012), and  $\sin^2 \theta_{13} = 0.0291 \pm 0.0035$  (stat)  $\pm 0.0051$  (sys) (RENO Collab., Ahn et al. 2012). The latter two results, because of their precision, effectively remove a degree of freedom from three-flavor solar neutrino analyses.

The mass differences and mixing angles from the global analyses of the Bari (Fogli et al. 2012) and Valencia (Forero, Tórtola & Valle 2012) groups, including experimental results through the Neutrino 2012 Conference, are shown in **Table 3**. The two analyses are generally in quite good agreement and yield (in degrees)

$$\theta_{12} \sim \begin{cases} 33.6^{+1.1}_{-1.0} \\ 34.4^{+1.0}_{-1.1} \end{cases} \quad \theta_{13} \sim \begin{cases} 8.96^{+0.45}_{-0.51} \\ 9.06^{+0.50}_{-0.57} \end{cases} \quad \begin{matrix} \text{Bari} \\ \text{Valencia} \end{matrix}. \quad (40)$$

The agreement in the solar neutrino mass difference  $\delta m_{21}$  is also excellent,

$$\delta m_{21}^2 \sim \begin{cases} (7.54^{+0.26}_{-0.22}) \times 10^{-5} \text{ eV}^2 \\ (7.62^{+0.19}_{-0.19}) \times 10^{-5} \text{ eV}^2 \end{cases} \quad \begin{matrix} \text{Bari} \\ \text{Valencia} \end{matrix}. \quad (41)$$

**Table 3 Results from global  $3\nu$  analyses including data through Neutrino 2012<sup>a</sup>**

Parameter/hierarchy	Bari Analysis (Fogli et al. 2012)			Valencia Analysis (Forero, Tórtola & Valle 2012)		
	Best $1\sigma$ Fit	$2\sigma$ Range	$3\sigma$ Range	Best $1\sigma$ Fit	$2\sigma$ Range	$3\sigma$ Range
$\delta m_{21}^2 (10^{-5} \text{ eV}^2)$	$7.54^{+0.26}_{-0.22}$	$7.15 \leftrightarrow 8.00$	$6.99 \leftrightarrow 8.18$	$7.62 \pm 0.19$	$7.27 \leftrightarrow 8.01$	$7.12 \leftrightarrow 8.20$
$\delta m_{31}^2 (10^{-3} \text{ eV}^2)\text{NH}$	$2.47^{+0.06}_{-0.10}$	$2.31 \leftrightarrow 2.59$	$2.23 \leftrightarrow 2.66$	$2.55^{+0.06}_{-0.09}$	$2.38 \leftrightarrow 2.68$	$2.31 \leftrightarrow 2.74$
IH	$-(2.38^{+0.07}_{-0.11})$	$-(2.22 \leftrightarrow 2.49)$	$-(2.13 \leftrightarrow 2.57)$	$-(2.43^{+0.07}_{-0.06})$	$-(2.29 \leftrightarrow 2.58)$	$-(2.21 \leftrightarrow 2.64)$
$\sin^2 \theta_{12}$	$0.307^{+0.018}_{-0.016}$	$0.275 \leftrightarrow 0.342$	$0.259 \leftrightarrow 0.359$	$0.320^{+0.016}_{-0.017}$	$0.29 \leftrightarrow 0.35$	$0.27 \leftrightarrow 0.37$
$\sin^2 \theta_{23}$ NH	$0.386^{+0.024}_{-0.021}$	$0.348 \leftrightarrow 0.448$	$0.331 \leftrightarrow 0.637$	$\begin{cases} 0.613^{+0.022}_{-0.040} \\ 0.427^{+0.034}_{-0.027} \end{cases}$	$0.38 \leftrightarrow 0.66$	$0.36 \leftrightarrow 0.68$
IH	$0.392^{+0.039}_{-0.022}$	$\begin{cases} 0.353 \leftrightarrow 0.484 \\ 0.543 \leftrightarrow 0.641 \end{cases}$	$0.335 \leftrightarrow 0.663$	$0.600^{+0.026}_{-0.031}$	$0.39 \leftrightarrow 0.65$	$0.37 \leftrightarrow 0.67$
$\sin^2 \theta_{13}$ NH	$0.0241 \pm 0.0025$	$0.0193 \leftrightarrow 0.0290$	$0.0169 \leftrightarrow 0.0313$	$0.0246^{+0.0029}_{-0.0028}$	$0.019 \leftrightarrow 0.030$	$0.017 \leftrightarrow 0.033$
IH	$0.0244^{+0.0023}_{-0.0025}$	$0.0194 \leftrightarrow 0.0291$	$0.0171 \leftrightarrow 0.0315$	$0.0250^{+0.0026}_{-0.0027}$	$0.020 \leftrightarrow 0.030$	$0.017 \leftrightarrow 0.033$

<sup>a</sup>Neutrino 2012 refers to The XXV International Conference on Neutrino Physics and Astrophysics held in Kyoto, Japan, June 3–9, 2012. Abbreviations: IH, inverted hierarchy; NH, normal hierarchy.

The values for  $\theta_{12}$  and  $\delta m_{21}^2$  lie in the LMA region of **Figure 6b**.  $\delta m_{21}^2$  corresponds, for 10-MeV neutrinos, to an MSW crossing density of  $\sim 20 \text{ g cm}^{-3}$  or, equivalently, a solar radius of  $r \sim 0.24R_{\odot}$ , which is the outer edge of the Sun’s energy-producing core. The crossing density for the atmospheric  $\delta m_{31}^2$ , again for 10-MeV neutrinos, is  $\sim 1.6 \times 10^3 \text{ g cm}^{-3}$ . Thus, this crossing requires electron densities far beyond those available in the Sun; however, it is typical of the carbon zone in the mantle of a Type II supernova, where this second crossing plays a significant role.

These global analysis results can be compared with those from the recent SNO three-flavor combined analysis, which used all available solar neutrino data and the results from KamLAND. This analysis, summarized in **Figure 7**, gives at  $1\sigma$

$$\sin^2 \theta_{12} = 0.308 \pm 0.014 \quad \delta m_{21}^2 = (7.41^{+0.21}_{-0.19}) \times 10^{-5} \text{ eV}^2 \quad \sin^2 \theta_{13} = 0.025^{+0.018}_{-0.015}. \quad (42)$$

These values are in excellent agreement with the corresponding  $1\sigma$  Bari and Valencia results of **Table 3**: The SNO combined analysis and Bari best values match particularly well. The main consequence of the inclusion of new reactor and accelerator results in the global analyses is a substantial reduction in the uncertainty on  $\theta_{13}$ .

## 5.2. Spectral Distortions: Low-Energy Threshold Analyses and Borexino

Characteristic spectral distortions are one of the signatures of oscillations in matter. Rather fortuitously, if Equation 34 is evaluated for the neutrino energy where the MSW critical density corresponds to the electron density at the center of the Sun,  $\rho \sim 6 \times 10^{25} \text{ cm}^{-3}$ , one finds  $E_{\text{crit}}^{\nu} \sim 1.9 \text{ MeV}$ , an energy in the center of the solar neutrino spectrum. Neutrinos below this energy will not experience a level crossing on exiting the Sun and, thus, will oscillate approximately as they would in vacuum, with an average (two-flavor) survival probability of

$$P_{\nu_e}^{\text{vacuum}} \sim 1 - \frac{1}{2} \sin^2 2\theta_{12} \sim 0.57, \quad (43)$$

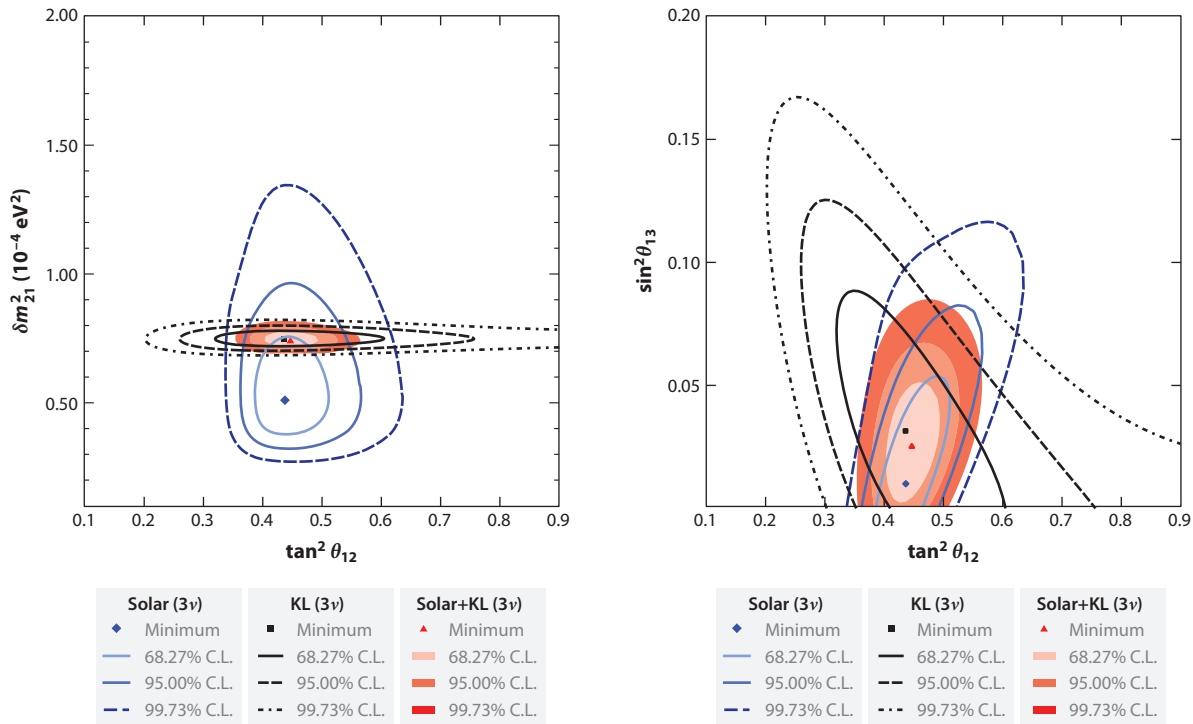


**Figure 7**

The three-flavor neutrino oscillation contours resulting from the Sudbury Neutrino Observatory (SNO) combined analysis: The analysis employs only solar neutrino and KamLAND data, but the results are in excellent agreement with the conclusions from global analyses that include recent reactor- and accelerator-neutrino constraints on  $\theta_{13}$ . Adapted from SNO Collab., Aharmim et al. (2012). Abbreviation: C.L., confidence limit; KL, KamLAND.

using  $\theta_{12} \sim 34^\circ$ . This can be compared to the matter-dominated survival probability, appropriate for neutrinos much above the critical energy,

$$P_{\nu_e}^{\text{high density}} \rightarrow \sin^2 \theta_{12} \sim 0.31. \quad (44)$$

Most of the  ${}^8\text{B}$  neutrinos studied by SNO and Super-Kamiokande undergo matter-enhanced oscillations. The matter/vacuum transition predicted by the MSW mechanism can be verified by comparing the survival probabilities of low-energy (pp or  ${}^7\text{Be}$ ) and high-energy ( ${}^8\text{B}$ ) neutrinos. Alternatively, if the thresholds in SNO and Super-Kamiokande are lowered sufficiently, spectral distortions will be detectable in the  ${}^8\text{B}$  spectrum: Low-energy  ${}^8\text{B}$  neutrinos coming from the outer core will not experience a crossing and, thus, will have a higher survival rate.

The flux of low-energy pp neutrinos is well constrained in global analyses because these neutrinos dominate the SAGE and GALLEX/GNO counting rates. (The need for an elevated survival probability for these neutrinos was an important factor in early model-independent analyses that concluded undistorted neutrino fluxes could not account for the data.) Furthermore, Borexino has now provided a direct, exclusive measurement at a precise energy, corresponding to the 860-keV neutrinos from  ${}^7\text{Be}$  EC.

To probe lower-energy  ${}^8\text{B}$  neutrinos, a joint reanalysis of Phase I and Phase II data from the SNO was carried out with an effective kinetic energy threshold of  $T_{\text{eff}} = 3.5$  MeV (SNO Collab., Aharmim et al. 2010). Although the low-energy threshold analysis (LETA) had several motivations

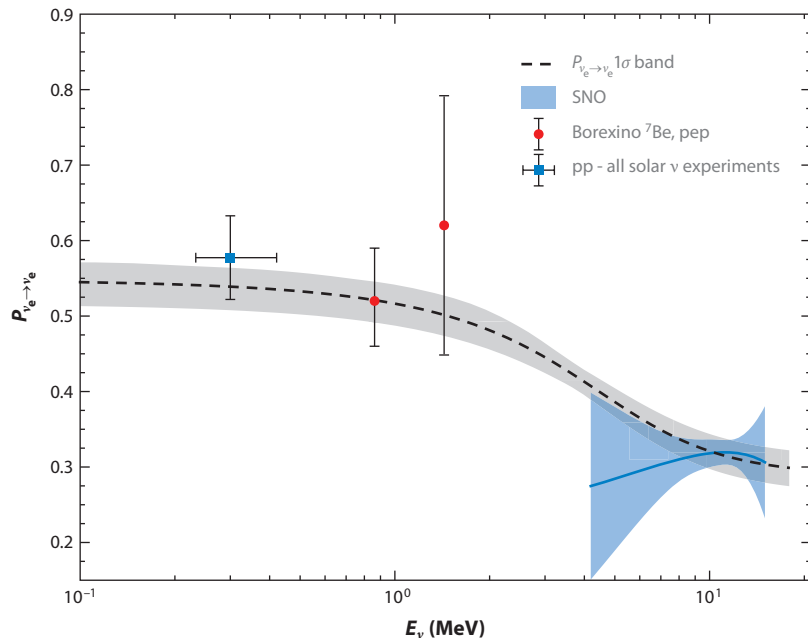


**Figure 8**

Survival probabilities  $P_{\nu_e}$  for proton-proton (pp), proton-electron-proton (pep),  ${}^7\text{Be}$ , and  ${}^8\text{B}$  neutrinos deduced from global solar neutrinos analyses, Borexino, and the Sudbury Neutrino Observatory (SNO) combined analysis, compared to the MSW prediction, taking into account present uncertainties on mixing angles. Adapted from SNO Collab., Aharmim et al. (2012), with pep result from Borexino Collab., Bellini et al. (2012a) added.

(e.g., the enlarged data set improved the overall precision of the flux determinations), a principal goal was enhancing prospects for detection of the predicted upturn in  $P_{\nu_e}$  with decreasing neutrino energy. An effort similar to the LETA is now underway in Super-Kamiokande IV. Preliminary results were recently described by Super-Kamiokande Collab., Smy et al. (2013).

**Figure 8** summarizes the data. The pattern defined by the pp  $\nu_e$  flux deduced from global analyses, the  ${}^7\text{Be}$   $\nu_e$  flux derived from the Borexino ES measurement, and the SNO results are generally in good agreement with the expected MSW survival probability. However, though the SNO LETA band is compatible with the MSW prediction, the band's centroid trends away from the theory with decreasing energy.

### 5.3. Day-Night Differences

Two sources of time variation in neutrino rates are the annual  $\sim 7\%$  modulation associated with the 1.7% eccentricity in Earth's orbit around the Sun, and the daily variation associated with terrestrial matter effects, which influence the night-time flux of up-going neutrinos. Both effects have been the subject of careful experimental studies [see, e.g., SNO Collab., Aharmim et al. (2005), Super-Kamiokande Collab., Smy et al. (2004)]. The integrated day-night asymmetry in neutrino detection rates

$$A_{\text{DN}} \equiv \frac{R_{\text{D}} - R_{\text{N}}}{\frac{1}{2}(R_{\text{D}} + R_{\text{N}})}, \quad (45)$$

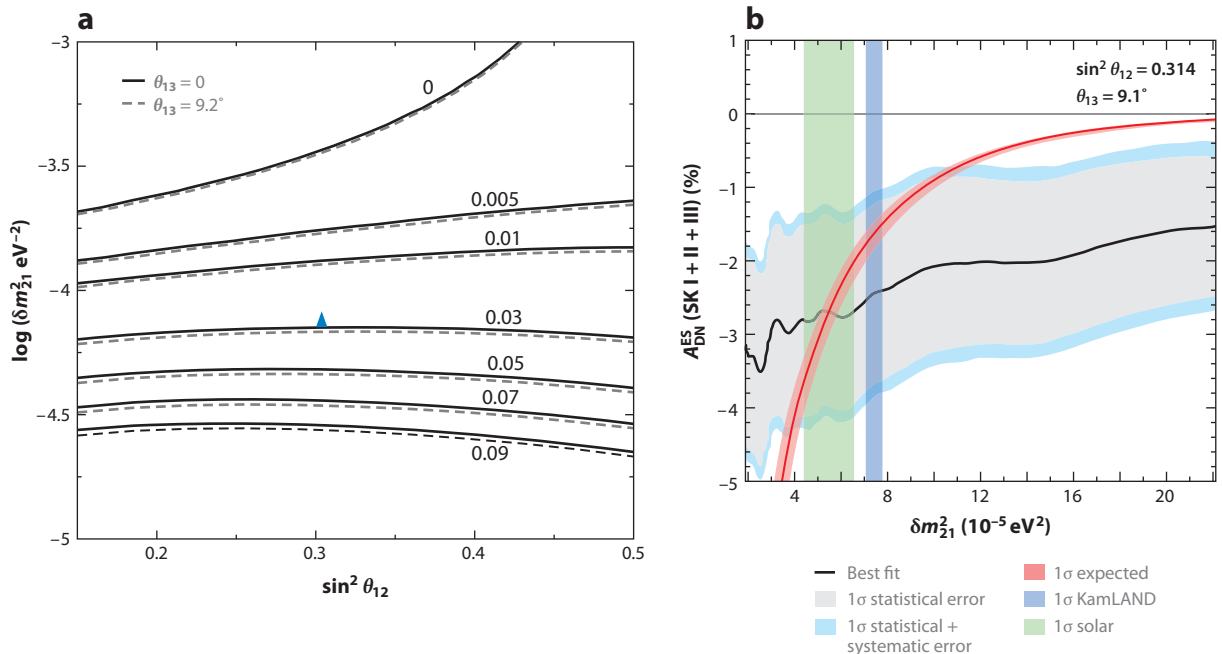


**Figure 9**

(a) The expected  $A_{\text{DN}}^{\text{ES}}$  for Super-Kamiokande as a function of  $\delta m_{21}^2$  and  $\sin^2 \theta_{12}$  for two (solid lines) and three (dashed lines,  $\theta_{13} = 9.2^\circ$ ) flavors. The lines are the contours of constant  $A_{\text{DN}}^{\text{ES}}$ . The blue triangle marks the best-fit parameters from current global analyses. Adapted from Blennow, Ohlsson & Snellman (2004). (b)  $A_{\text{DN}}^{\text{ES}}$  values consistent with current values of  $\theta_{12}$  and  $\theta_{13}$  (red band), plotted as a function of  $\delta m_{21}^2$ , compared to SKI + II + III results ( $1\sigma$  statistical and statistical + systematic errors indicated). The vertical bands are the  $1\sigma$  KamLAND and solar values for  $\delta m_{21}^2$ . Adapted from A. Renshaw and M. Smy (private communication).

where  $R_{\text{D}}$  and  $R_{\text{N}}$  denote the day and night rates, is the quantity most often studied to assess matter effects associated with solar neutrino passage through Earth. In principle, similar differential quantities could be defined as functions of the neutrino energy and zenith angle. However, the detection of even the integrated difference  $R_{\text{DN}}$  is statistically challenging because the effect is expected to be only a few percent.

$A_{\text{DN}}$  provides an “on-off” test where the matter effects can be measured directly, unlike the solar case where matter effects must be deduced from phenomena such as spectral distortions. The magnitude of the neutrino regeneration associated with passage through Earth depends on the neutrino energy, the assumed oscillation parameters, and, to some extent, detector location because that determines the possible trajectories through Earth to the Sun.

The high counting rate of Super-Kamiokande is an advantage in constraining the contribution to  $A_{\text{DN}}$  from the high-energy  $^8\text{B}$  neutrinos. The expected Super-Kamiokande ES  $A_{\text{DN}}$  is illustrated in **Figure 9** as a function of  $\delta m_{21}^2$  and  $\sin^2 \theta_{13}$  in the two- and three-flavor cases. For the current global best-fit parameters, the effect should be about  $-3\%$ . The results for the four phases

$$\begin{array}{llll}
 -2.1 \pm 2.0 \pm 1.3\% & \text{SK I} & 6.3 \pm 4.2 \pm 3.7\% & \text{SK II} \\
 -5.9 \pm 3.4 \pm 1.3\% & \text{SK III} & -5.2 \pm 2.3 \pm 1.4\% & \text{SK IV (preliminary)}
 \end{array} \quad (46)$$

yield a combined result of  $A_{\text{DN}}^{\text{ES}}(\text{SK}) = -4.0 \pm 1.3 \pm 0.8$ , in good agreement with expectations but still consistent with no effect at  $2.6\sigma$  (Super-Kamiokande Collab., Smy et al. 2013).

The SNO Collaboration has analyzed day-night effects in the  $\nu_e$  channel in their combined analysis, approximating the effect as linear in  $E_\nu$ ,

$$A_{\text{DN}}^{\nu_e}(\text{SNO}) = -a_0 - a_1 \left( \frac{E_\nu}{10 \text{ MeV}} - 10 \right). \quad (47)$$

The null hypothesis that there are no day-night effects influencing the  $\nu_e$  survival probability (so  $a_0 = 0, a_1 = 0$ ) yielded a  $\Delta\chi^2 = 1.87$  (61% C.L.) compared with the best fit (SNO Collab., Aharmim et al. 2012). The Borexino result for the ES at 862 keV (Borexino Collab., Bellini et al. 2012b),

$$A_{\text{DN}}^{\text{ES}}(862 \text{ keV}) = -(0.001 \pm 0.012 \pm 0.007), \quad (48)$$

is consistent with the expectation that  $|A_{\text{DN}}^{\text{ES}}(862 \text{ keV})| \lesssim 0.001$  for the LMA solution at this energy.

## 6. NEUTRINO CONSTRAINTS ON SOLAR STRUCTURE

One of the important consequences of the increasingly precise understanding of neutrino flavor physics is the opportunity to return to one of the early goals of solar neutrino spectroscopy: using the neutrino as a probe of the physics of the solar interior. Neutrino fluxes, sensitive to nuclear reaction rates and core temperature, can be combined with helioseismic observations, which are sensitive to radiative opacities and microscopic diffusion, to place stringent constraints on the SSM and to test some of its implicit assumptions. This program is of broad significance to stellar astrophysics because the SSM is a particular application of the general theory of main-sequence stellar evolution. Because we know the Sun's properties far better than those of any other star, the SSM provides one of our best opportunities to test that theory against precise data and, thus, to identify shortcomings.

A decade ago, the SSM was in spectacular agreement with observations apart from solar neutrino data, a fact that supported suggestions that the solar neutrino problem might have a nonsolar origin. However, as the SSM makes a number of simplifying assumptions, it is perhaps inevitable that some experimental test of our Sun will eventually demonstrate the model's shortcomings. Over the past decade, the development of 3D hydrodynamic models of near-surface solar convection, a more careful selection of spectral lines, and, in some cases, relaxation of the assumption of local thermodynamic equilibrium in line formation have led to significant changes in the analysis of data on photospheric absorption lines. The most recent revisions reduced the abundances of the volatile CNO elements and Ne by  $\sim 0.10$ – $0.15$  dex (equivalently, by  $\sim 25$ – $40\%$ ), relative to older compilations of solar abundances; however, significant debate continues. The differences between the new AGSS09 and the older GS98 abundances can be summarized in the respective total metal-to-hydrogen ratios of  $(Z/X)_\odot \sim 0.018$  and  $0.023$ , respectively. As the SSM assumes a homogeneous zero-age composition, adoption of the AGSS09 abundances produces a modern Sun with a lower core metallicity, affecting solar neutrino flux predictions and substantially degrading the agreement between the SSM sound velocity profile and that deduced from helioseismology.

### 6.1. The Solar Abundance Problem and Its Standard Solar Model Implications

Past studies of SSMs with low  $Z/X$  interiors similar to that of the AGSS09-SFII SSM have revealed a number of difficulties with respect to observation: the radius of the convective zone boundary  $R_{\text{CZ}}$ , the interior sound speed and density profiles, and the surface He abundance  $Y_\odot$  all move outside the ranges determined from helioseismic analyses (Bahcall, Serenelli & Pinsonneault 2004; Basu &

Antia 2004; Montalban et al. 2004). These changes reflect the increase in the efficiency of radiative transport and decrease in core molecular weight found in low- $Z$  models. For example,  $R_{CZ}$  moves outward in low- $Z$  models because radiative transport dominates over a larger fraction of the solar interior. Similarly,  $Y_S$  decreases: As SSM energy generation is fixed by the measured luminosity  $L_\odot$ , the cooler core in low- $Z$  models must be compensated by an increase in the available fuel  $X$ , and consequently a lower core  $Y$  and, thus, surface  $Y_S$ . In addition, the low initial helium abundance, though not in conflict with Big Bang nucleosynthesis, leads to a helium-to-metal enrichment ratio  $\Delta Y/\Delta Z = 0.8$  that is much lower than observational estimations ranging between  $\sim 1.4$  and  $2.5$  and is also in disagreement with the initial helium abundance,  $Y_{\text{ini}} = 0.273 \pm 0.006$ , derived by Serenelli & Basu (2010) using the seismic  $Y_S$  and a wide range of SSMs and nonstandard solar models (NSSMs). In contrast, SSM predictions using the older, high- $Z$  GS98 abundances are in much better agreement with observation. (See **Table 1** and **Figure 5**.) The inconsistency between the SSM parameterized using the best current description of the photosphere (AGSS09 abundances) and the SSM parameterized to optimize agreement with helioseismic data sensitive to interior composition (GS98 abundances) is known as the solar abundance problem.

The solar abundance problem could have a pedestrian solution: The 3D analysis by Caffau et al. (2008, 2009, 2010) yielded abundances higher than the AGSS09 values, though this appears to be due to spectral line choices rather than photospheric model differences (Grevesse et al. 2011), a conclusion supported by a recent comparison between solar model atmospheres computed by different groups (Beeck et al. 2012). Alternatively, an upward adjustment in associated atomic opacities could compensate for a low- $Z$  interior, if some justification for such a change could be identified.

However, the solar abundance problem could be more fundamental. An important assumption of the SSM—a homogeneous zero-age Sun—is not based on observation, but instead on the theoretical argument that the proto-Sun likely passed through a fully convective Hayashi phase as the presolar gas cloud collapsed, thereby destroying any composition inhomogeneities that might have existed. Yet we know that chemical inhomogeneities were re-established during Solar System formation: Processes operating in the protoplanetary disk removed  $\sim 40\text{--}90 M_\oplus$  of metal from the gas, incorporating this material in the gaseous giants (Guillot 2005). The gas from which these metals were scoured—representing perhaps the last  $\sim 5\%$  of that remaining in the disk—would have been depleted in metal and enriched in H and He. The fate of that gas is unknown, but if it were accreted onto the Sun, it plausibly could have altered the composition of the convective zone, depending on the timing of the accretion and, thus, the maturity of the proto-Sun's growing, chemically segregated radiative core. That is, as there is a candidate mechanism for altering the convective zone late in protosolar evolution, involving enough metal to account for the AGSS09/GS98 differences, it is not obvious that the SSM assumption of homogeneity is correct.

The solar abundance problem has the three following connections to neutrinos:

1. Neutrino fluxes are sensitive to metallicity and, thus, can be used to cross-check the conclusions drawn from helioseismology. Below we describe what the neutrino fluxes currently tell us.
2. Neutrino fluxes place important constraints on NSSMs motivated by the solar abundance problem, such as those recently developed to explore accretion from the protoplanetary disk.
3. Planned measurements (Chen 2006, Franco 2011) of the CN solar neutrino flux have the potential to directly measure the solar core abundance of C + N with a precision that will impact the solar abundance problem.

In principle the temperature-dependent  $^8\text{B}$  and  $^7\text{Be}$  neutrino fluxes have sufficient sensitivity to metallicity to impact the solar abundance debate. As **Table 2** shows, the AGSS09-SFII and

GS98-SFII SSMs differ by 21.6% and 9.6% in their  $^8\text{B}$  and  $^7\text{Be}$  flux predictions, respectively, which one can compare to the 14% and 7% SSM uncertainties on these fluxes obtained by varying SSM input parameters according to their assigned errors. These total SSM uncertainties were determined by adding in quadrature the individual uncertainties from 19 SSM input parameters, including abundance uncertainties as given in the respective solar abundance compilations. In the case of the  $^8\text{B}$  flux, the important uncertainties include those for the atomic opacities (6.9%), the diffusion coefficient (4%), the nuclear S-factors for  $^3\text{He} + ^4\text{He}$  (5.4%) and  $^7\text{Be} + \text{p}$  (7.5%), and the Fe abundance (5.8%).

Unfortunately, the current neutrino data do not favor either abundance set. The last entries in **Table 2** give the  $\chi^2$  functions and compatibility functions  $P^{\text{gr}}$  obtained in the SSM for the two sets, following Gonzalez-Garcia, Maltoni & Salvado (2010) but using the updated Solar Fusion II S-factors. The two models are identical in quality of fit to the data, with  $\chi_{\text{AGSS09-SFII}}^2 = 3.4$  and  $\chi_{\text{GS98-SFII}}^2 = 3.5$ . In **Table 2**, one sees that a SSM model intermediate in metallicity between AGSS09 and GS98 would optimize the agreement.

## 6.2. Solar Models with Accretion

Guzik (2006), Castro, Vauclair & Richard (2007), and Guzik & Mussack (2010) considered the possibility that the solar abundance problem might be due to accretion of metal-poor matter onto the Sun's convective envelope, diluting its presolar composition. Haxton & Serenelli (2008) suggested the mechanism for such dilution described above, accretion of disk gas from which the metals were previously scoured in the process of planetary formation. Evidence supporting the hypothesis that planetary formation could affect the surface metallicity of the host star was offered by Melendez et al. (2009), who found that the peculiar differences in the surface abundances of the Sun, measured relative to similar stars (solar twins), correlate with condensation temperatures and, thus, plausibly with disk chemistry. Nordlund (2009) argued this accretion scenario might also provide a natural explanation for the anomalous metallicity of Jupiter.

Although the process of planetary formation is not well understood, the standard picture invokes a chemically differentiated thin disk, with dust, ice, and thus metals concentrated in the midplane, and outer surfaces dominated by H and He. This configuration arises from a combination of gas cloud collapse that is rapid at the poles but inhibited by angular momentum at the equator and gas cooling that allows differential condensation of various elements as ice or grains according to their condensation temperatures. The formation of planetesimals in the midplane and their self-interactions lead to the formation of rocky cores of planets. The gas giants, which are sufficiently distant from the Sun that ice can augment their cores, reach masses where tidal accretion of gas can further feed their growth.

The implications of this disk chemistry for solar initial conditions are difficult to assess because of a number of uncertain parameters. Although we know the planets are substantial metal reservoirs, we do not know the fate of the depleted gas that dominates the disk surface: It might have been removed by the solar wind or, alternatively, deposited on the Sun through magnetospheric mechanisms, such as those operating in young accreting T Tauri stars. If accretion occurs, its timing relative to early solar evolution is critical. The timescale for planetary formation is generally estimated at 1–10 Myr, whereas the SSM predicts that the early Sun's convective boundary moves outward, in response to the growing radiative core, over a longer period of  $\tau_{\text{CZ}} \sim 30$  Myr. If accretion occurs early in this period, when most of the Sun's mass is in its convective envelope, any resulting nonuniformity in solar abundances would be negligible. But if accretion occurs later when the convective zone is similar to that of the modern Sun, and thus contains only  $\sim 2\%$  of the Sun's mass, the chemical processing of  $\sim 0.05M_{\odot}$  of gas, dust, and ice in the planetary nebula

could have very significant consequences. Alternatively, as suggested by hydrodynamic simulations of the contraction of the protosolar nebula (Wuchterl & Klessen 2001) and stellar models that include episodic accretion during the pre-main-sequence phase with large mass accretion rates (Baraffe & Chabrier 2010), the Sun may have avoided the fully convective phase altogether. Finally, the mass and composition of the accreted material are highly uncertain. Because condensation temperatures for the elements vary widely—e.g., from  $\sim 1,400$  K for Fe to  $\sim 300$  K for C—the composition would likely evolve with time as the disk cools.

Motivated in part by such considerations, a NSSM was recently developed to test whether early accretion from a planetary disk could resolve the solar abundance problem (Serenelli, Haxton & Peña-Garay 2011). The work illustrates the importance of neutrino physics in limiting NSSMs. In SSMs, the presolar composition parameters  $Y_{\text{ini}}$  and  $Z_{\text{ini}}$  as well as the mixing length parameter  $\alpha_{\text{MLT}}$  are determined by iterating the model to reproduce the present-day solar luminosity  $L_{\odot}$ , radius  $R_{\odot}$ , and surface metal-to-hydrogen ratio  $Z_{\text{S}}/X_{\text{S}}$ . This algorithm was modified for the accreting NSSM by allowing for a mass  $M_{\text{ac}}$  of accreted material with fixed composition ( $X_{\text{ac}}, Y_{\text{ac}}, Z_{\text{ac}}$ ), deposited on the early Sun uniformly, beginning at time  $\tau_{\text{ac},i}$  and lasting a time  $\Delta\tau_{\text{ac}}$ . Prior to time  $\tau_{\text{ac},i}$  the Sun was evolved as a SSM with mass  $M_{\odot} - M_{\text{ac}}$  and composition defined by ( $X_{\text{ini}}, Y_{\text{ini}}, Z_{\text{ini}}$ ). During the subsequent accretion phase, the simplifying assumption  $X_{\text{ac}}/Y_{\text{ac}} \equiv X_{\text{ini}}/Y_{\text{ini}}$  was made. For a given set of fixed accretion parameters,  $Y_{\text{ini}}, Z_{\text{ini}}$ , and  $\alpha_{\text{MLT}}$  were then adjusted iteratively in order to reproduce  $L_{\odot}, R_{\odot}$ , and  $Z_{\text{S}}/X_{\text{S}}$ , as in the SSM. Thus,  $Y_{\text{ini}}, Z_{\text{ini}}$ , and  $\alpha_{\text{MLT}}$  become functions of the assumed accretion parameters so that in place of a single SSM solution, a family of solutions is obtained with different interior compositions. Unphysical solutions are rejected, e.g., the AGSS09  $Z_{\text{S}}/X_{\text{S}}$  is not compatible with the accretion of large quantities of metal-rich material at late times, when the convective envelope is thin.

**Figure 10** shows the helioseismic consequences of late accretion—accretion onto a young Sun with a thin convective envelope similar to that of the modern Sun. Also shown are the variations in  $Y_{\text{ini}}$  and  $Z_{\text{ini}}$ , the initial core He and heavy-element mass fractions, that can be achieved through accretion. The helioseismic observables are very constraining. The candidate accretion solution to the solar abundance problem that one might naively envision—a low- $Z$  surface consistent with AGSS09 and an interior similar to GS98, with higher  $Z_{\text{ini}} \sim 0.019$  and  $Y_{\text{ini}} \sim 0.28$ —can be achieved with metal-free and metal-poor accretion involving modest accreted masses  $M_{\text{ac}} \sim 0.01 M_{\odot}$ . These models bring  $Y_{\text{S}}$  into good agreement with observation and produce some improvement in the sound-speed figure-of-merit ( $\delta c/c$ ). But the lower  $Z_{\text{S}}$  that accompanies metal-free/metal-poor accretion allows the convective zone radius to move outward, exacerbating the existing AGSS09-SFII SSM helioseismic discrepancy in  $R_{\text{S}}$ .

Neutrino flux measurements impose a second class of constraints on accreting NSSMs. The scenario discussed above—metal-free or metal-poor accretion with  $M_{\text{ac}} \sim 0.01 M_{\odot}$ —can marginally improve the agreement with neutrino data, as the best fit requires a core metallicity midway between the AGSS09 and GS98 values. But with larger  $M_{\text{ac}}$ , the agreement quickly deteriorates because the resulting high- $Z$  interior leads to rapid increases in the  ${}^8\text{B}$  and  ${}^7\text{Be}$  neutrino fluxes. The power of contemporary neutrino flux measurements to constrain NSSMs is quite remarkable. Large classes of accretion parameters—mass, time, composition, and duration—lead to modern Suns with the proper luminosity and radius and the AGS009  $Z_{\text{S}}$  while still satisfying the underlying equations of stellar structure. Yet, very few of these solutions produce acceptable neutrino fluxes, as **Figure 11** illustrates.

Effectively, the recent progress made on neutrino mixing angles and mass differences has turned the neutrino into a well-understood probe of the Sun. We now have two precise tools, helioseismology and neutrinos, that can be used to see into the solar interior, complementing the more traditional astronomy of solar surface observations. We have come full circle: The

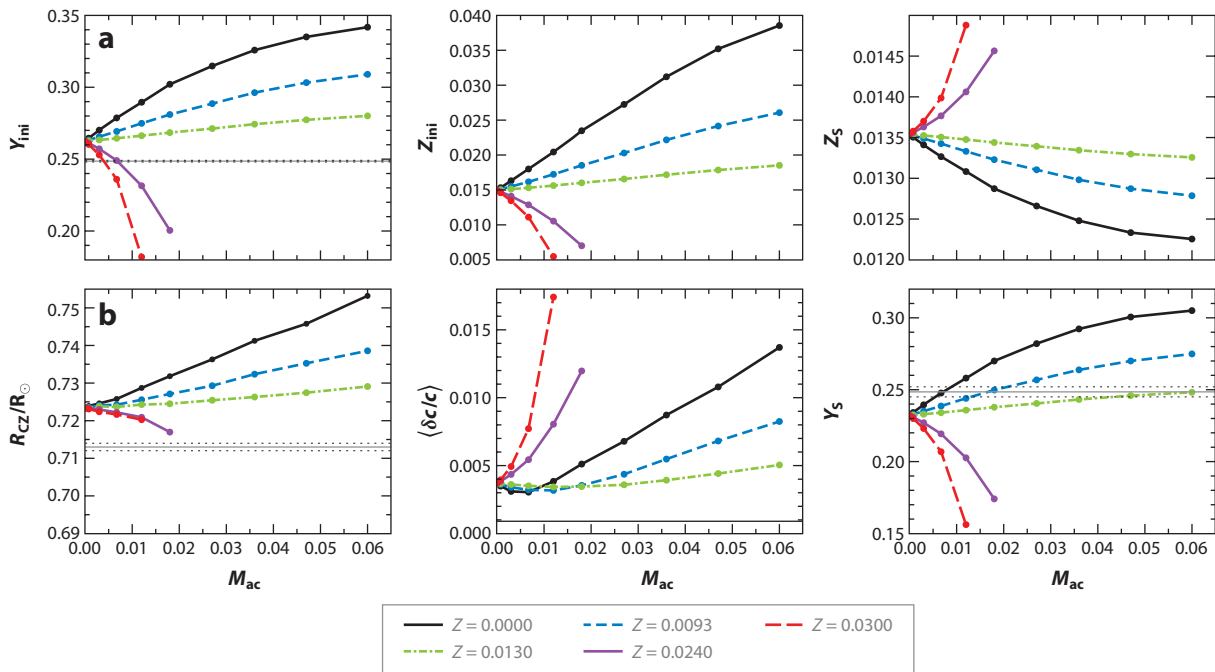


**Figure 10**

Accretion on a young Sun with a thin convective envelope as a function of the mass and metallicity of the accreted material. (a) The deduced He and metal content of the presolar gas,  $Y_{\text{ini}}$  and  $Z_{\text{ini}}$ , and present-day  $Z_S$ , determined from the luminosity, radius, and AGSS09 photospheric  $Z_S/X_S = 0.0178$  constraints. Truncated trajectories indicate the absence of a physical solution. (b) A comparison of the resulting helioseismic properties of the models to observation (*horizontal bands*).

Homestake experiment was to have been a measurement of the solar core temperature, until the solar neutrino problem intervened.

### 6.3. Neutrinos as a Direct Probe of Solar Composition: SNO+

Although solar fusion is dominated by the pp chain, the CN cycle generates  $\sim 1\%$  of solar energy as well as  $^{13}\text{N}$  and  $^{15}\text{O}$  neutrino fluxes of  $2.96$  ( $2.17$ ) and  $2.23$  ( $1.56$ )  $\times 10^8 \text{ cm}^{-2} \text{ s}^{-1}$ , respectively, for the GS98-SFII (AGSS09-SFII) SSM. These fluxes can be measured in scintillation detectors in an energy window of 800–1,400 keV, provided backgrounds in the detectors are reduced to acceptable levels, including in particular interference from the decay of  $^{11}\text{C}$  produced by penetrating muons. Borexino has already established a limit on the CN fluxes and is pursuing strategies to improve the measurement by vetoing interfering backgrounds (Franco 2011). A new scintillation detector under construction in the cavity previously occupied by SNO will have three times the volume of Borexino and 1/70th the muon background, due to SNOLAB's 2-km depth (Chen 2006). A SNO + CN neutrino signal/ $^{11}\text{C}$  background of  $\sim 10$  is expected.

A measurement of the CN neutrinos would test our understanding of hydrogen fusion as it occurs in main-sequence stars substantially more massive than the Sun. It could also play an important role in the solar abundance problem.

The CN neutrino fluxes, like the  $^8\text{B}$  and  $^7\text{Be}$  neutrino fluxes, depend sensitively on core temperature  $T_C$  and, thus, respond to variations in SSM input parameters that affect  $T_C$ . But in

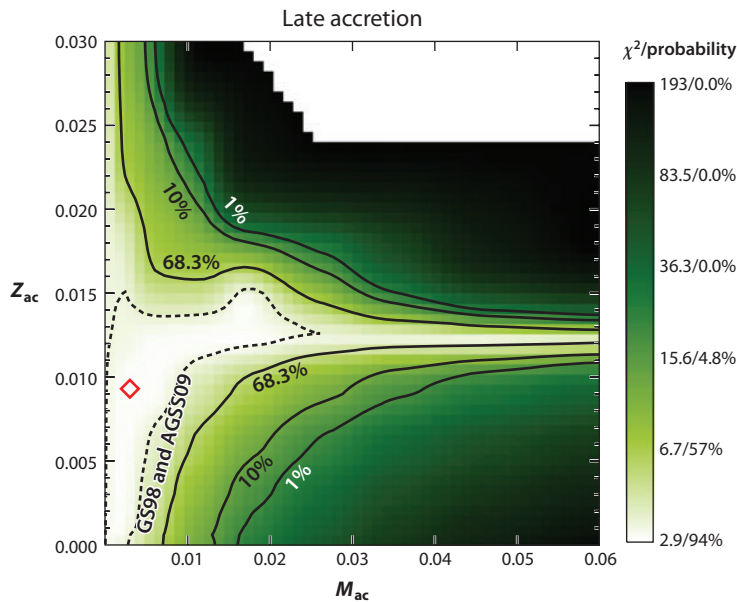


**Figure 11**

Global  $\chi^2$  solar neutrino analysis for the late accretion nonstandard solar model (NSSM) scenario. Contours are shown for 1%, 10%, and 68.4% confidence, with the best-fit model indicated by the red diamond. The fixed  $\chi^2$  contours corresponding to the AGSS09-SFII and GS98-SFII SSM fits are overlaid, showing the very limited parameter space where NSSMs with accretion do better than SSMs.

addition, the CN fluxes have a linear dependence on the presolar core abundances of C and N that is unrelated to  $T_C$ , reflecting the proportionality of CN neutrino fluxes to the abundances that catalyze the hydrogen burning. The  $T_C$  power-law relationships for the CN and  $^8\text{B}$  neutrino fluxes and the additional linear dependence of the CN neutrino flux on the abundance of C + N can be exploited to relate solar neutrino measurements to the Sun's presolar C and N abundances (Haxton & Serenelli 2008)

$$\frac{\phi(^{15}\text{O})}{\phi(^{15}\text{O})_{\text{SSM}}} = \left[ \frac{\phi(^8\text{B})}{\phi(^8\text{B})_{\text{SSM}}} \right]^{0.729} x_{\text{C+N}} \times [1 \pm 0.006(\text{solar}) \pm 0.027(D) \pm 0.099(\text{nucl}) \pm 0.032(\theta_{12})] \quad (49)$$

where  $x_{\text{C+N}}$  is the C + N number abundance normalized to its SSM value. The uncertainties were derived from SSM logarithmic derivatives, as described in Section 2. The first two of these represent variations in all SSM parameters—other than the nuclear cross sections—including  $L_\odot$ , the opacity, solar age, and all abundances other than C and N, using abundance uncertainty intervals of

$$x_j \equiv 1 \pm \left| \frac{\text{Abundance}_i^{\text{GS98}} - \text{Abundance}_i^{\text{AGSS09}}}{(\text{Abundance}_i^{\text{GS98}} + \text{Abundance}_i^{\text{AGSS09}})/2} \right|. \quad (50)$$

Apart from the diffusion parameter  $D$ , the net effect of the variations in these quantities is an uncertainty of 0.6%: We have formed a ratio of fluxes that is effectively insensitive to  $T_C$ . The diffusion parameter  $D$  is an exception because our expression relates contemporary neutrino flux measurements to the presolar number densities of C and N; thus, our expression must be corrected

for the effects of diffusion over 4.6 Gyr. The differential effects of diffusion on the ratio create an uncertainty of 2.7%, the only significant nonnuclear solar uncertainty.

Equation 49 is written for instantaneous fluxes and, thus, must be corrected for the energy-dependent effects of oscillations. The SNO combined analysis result  $\theta_{12} = 34.06_{-0.84}^{+1.16}$ —or equivalently the Bari or Valencia global analysis results discussed in Section 5—imply a  $\lesssim 3.2\%$  uncertainty in the flux comparison of Equation 49. Finally, there are nuclear physics uncertainties. These dominate the overall error budget, with the combined (in quadrature) error reflecting a 7.2% uncertainty from the  $^{14}\text{N}(p, \gamma)$  reaction and a 5.5% uncertainty from  $^7\text{Be}(p, \gamma)$ .

The SNO and Super-Kamiokande measurements of the  $^8\text{B}$  flux have reached a precision of 3%. SNO+ has the potential to measure the  $^{15}\text{O}$  flux to about 7% in three years of running. Assuming such a result from SNO+ and combining all errors in quadrature, the presolar C + N abundance can be determined to  $\pm 13\%$ . The precision could be improved substantially by addressing the uncertainties in the S-factors  $S_{114}$  and  $S_{17}$ . But even without such improvements, the envisioned SNO+ result would have a major impact, given the existing  $\sim 30\%$  differences in the AGSS09 and GS98 C and N abundances.

## 7. OUTLOOK AND CHALLENGES

The saga of solar neutrinos began 50 years ago with the straightforward goal of testing Bethe's idea of how the Sun makes its energy through the fusion of protons (Bethe & Critchfield 1938). The Sun's energy output leads immediately to a prediction for the total flux of neutrinos with a precision of a few percent. But detecting neutrinos is no simple matter, and the total flux cannot be measured directly. The neutrino spectrum must also be known in order to interpret experimental results. This vastly more difficult theoretical question led to the development of what is now known as the SSM. The theory could not be perfected and made predictive without laboratory data. The solar luminosity, mass, and age; nuclear reaction cross sections; elemental abundances; and radiative opacities were needed. Teams of astronomers, astrophysicists, atomic physicists, nuclear physicists, satellite design engineers, and theorists of many specializations turned to the task.

The fact that theory and experiment were not in agreement became increasingly apparent in the early 1970s, when the statistical accuracy of Davis's Cl-Ar experiment continued to improve as additional runs were completed and as multiple checks and calibrations were performed. The solar neutrino problem, as it became known, engendered spirited debate. Is it the SSM or some experimental error, or could it be neutrino oscillations?

The detection of solar neutrinos has now been achieved in eight detectors: the original Davis Cl-Ar experiment, Kamiokande, SAGE, GALLEX/GNO, Super-Kamiokande, SNO, Borexino, and KamLAND. By the mid-1990s some tension had developed between the pure CC data from Cl-Ar, SAGE, and GALLEX/GNO and the elastic-scattering data from Kamiokande and Super-Kamiokande. The neutrino-oscillation solution alone could eliminate that tension because of the NC component of ES. Finally, with spectrally selective observation of a single source ( $^8\text{B}$  neutrinos) using a detector capable of CC, ES, and NC discrimination (SNO), there remained no doubt that oscillations were the resolution of the solar neutrino problem.

The implications for neutrino physics and for solar astrophysics were both profound. Electron neutrinos were shown to participate in mixing and oscillations like their mu and tau cousins, and the masses of all three mass eigenstates were tied together by experimental data. The laboratory upper limit on neutrino mass dropped immediately from tens of kiloelectronvolts to 2.3 eV, the limit from tritium beta decay, and a lower limit on the average neutrino mass lay no more than two orders of magnitude below that. The mixing angle  $\theta_{12}$  was precisely determined from solar

neutrino data. The existence of MSW matter enhancement was confirmed, and the sign of the mass-squared difference  $\Delta m_{12}^2$  determined.

The astrophysical theory embodied in the SSM was shown to have correctly predicted the central temperature of the Sun to a precision of 1%, an achievement made all the more stunning by the fact that it appeared for decades to disagree with data.

The field of solar neutrinos has metaphorically paused to take a breath. What are the next steps? The experimental challenge ahead is clear: a comparison of the Sun's electromagnetic luminosity and neutrino luminosity with a precision of 1%. There are two scientific objectives, as we describe below.

Most Sun-like stars are somewhat variable, but solar variability is certainly not large. However, it might not be negligible, and some evidence for it can be found in the sunspot record. The Maunder minimum in the seventeenth century was accompanied by abnormally cold temperatures in Europe. The role of solar forcing is central to a complete understanding of climate change. Neutrinos reach Earth 8 min after they are created in the core of the Sun, whereas thermal energy takes thousands of years to travel from a hypothetical zone of variability within the Sun to the solar surface. We thus have an opportunity to make a measurement of the Sun's true energy production rate and compare it with its current rate of energy delivery. Modern satellite instruments record the latter with a precision of parts in  $10^4$ .

The second objective of a precision measurement of the neutrino luminosity springs from the fact that the solar neutrino spectrum is so well understood that it can be used as a standard candle to search for neutrino oscillation and separate it into sterile flavors that have been posited (Abazajian et al. 2012) or to search for the influence of nonstandard interactions (Biggio, Blennow & Fernandez-Martinez 2009). A disagreement between the neutrino luminosity and the electromagnetic luminosity could possibly be interpreted (depending on the sign) in terms of solar variability or neutrino physics and would call for other kinds of experiments to make the distinction.

An experimental measurement of the neutrino luminosity to 1% is difficult but not out of reach. Most of the flux is in the pp spectrum, and the other spectral components have already been measured or limited almost to the accuracy needed (Gonzalez-Garcia, Maltoni & Salvado 2010). The pep neutrinos may serve as a more experimentally accessible surrogate for the pp neutrinos, introducing very modest model dependence. Correction for neutrino oscillations requires knowledge of  $\theta_{12}$  to an accuracy of a factor about two better than presently known, and  $\theta_{13}$  is already adequately determined. One component of the solar flux is currently experimentally inaccessible: the thermal flux (Haxton & Lin 2000), a solar source that becomes significant below 10 keV, with a peak flux density of  $\sim 10^9 \text{ cm}^{-2} \text{ s}^{-1} \text{ MeV}^{-1}$ . Neutrinos of all flavors are produced by various  $Z_0 \rightarrow \nu\bar{\nu}$  processes operating in the Sun. This flux is a loss mechanism that slightly modifies the luminosity constraint.

The detection of pp or pep neutrinos in an experiment such as LENS (Low-Energy Neutrino Spectroscopy) (Grieb et al. 2011) would check the luminosity condition at an interesting level of precision. An absolute measurement at the 1% level, however, is difficult for an experiment that requires an auxiliary calibration with a powerful radioactive source. Making use of the precisely known cross section for ES of neutrinos from electrons avoids that step. Such experiments have been explored; the HERON (Helium Roton Observation of Neutrinos) project based on inherently very pure liquid helium (Huang et al. 2008) is one example, and CLEAN (Cryogenic Low Energy Astrophysics with Neon), based on liquid neon (McKinsey & Coakley 2005), is another.

Exciting as it is to contemplate this next step, in the new-precision era, theory remains as important and challenging as experiment. What are the implications of the metallicity problem? A measurement of the CN flux with 10% precision would be enormously valuable in guiding us and might be within reach for the SNO+ detector, along with the  ${}^7\text{Be}$  and pep components.

For all its successes, the SSM leaves out much that may be important. Can rotation, magnetic fields, evolutionary effects in the collapsing presolar nebula, and the influence of the formation of planets be incorporated? Just as the SSM allowed us to exploit our best-understood star to test the general theory of main-sequence stellar evolution, an effort to develop a standard Solar System model—one including gas cloud collapse, disk formation and accretion, realistic presolar evolution, the growth of planets, and the coupled astrochemistry of the Sun and planets—could provide a needed template for interpreting what we are now learning about exoplanets and their host stars.

## DISCLOSURE STATEMENT

The authors are not aware of any affiliations, memberships, funding, or financial holdings that might be perceived as affecting the objectivity of this review.

## ACKNOWLEDGMENTS

We are very grateful to Michael Smy for several helpful discussions on Super-Kamiokande. This work was supported in part by the US Department of Energy under contracts DE-SC00046548 (UC Berkeley), DE-AC02-98CH10886 (LBNL), and DE-FG02-97ER41020 (CENPA, Univ. Washington). A.M.S. is partially supported by the European Union International Reintegration Grant PIRG-GA-2009-247732, the MICINN grant AYA2011-24704, the ESF EUROCORES Program EuroGENESIS (MICINN grant EUI2009-04170), the SGR grants of the Generalitat de Catalunya, and EU-FEDER funds.

## LITERATURE CITED

- Abazajian KN, Acero MA, Agarwalla SK, Aguilar-Arevalo AA, Albright CH, et al. 2012. (arXiv:1204.5379)
- Abazajian KN, Calabrese E, Cooray A, De Bernardis F, Dodelson S, et al. 2011. *Astropart. Phys.* 35:177
- Adelberger EG, Austin S, Bahcall J, Balantekin A, Bogaert G, et al. 1998. *Rev. Mod. Phys.* 70:1275
- Adelberger EG, García A, Robertson RG, Snover KA, Balantekin AB, et al. 2011. *Rev. Mod. Phys.* 83:195
- Akhmedov EK. 1988. *Phys. Lett. B* 213:64
- Alvarez LW. 1949. *Lawrence Radiat. Lab. Phys. Notes Memo #767*
- Appourchaux T, Belkacem K, Broomhall AM, Chaplin WJ, Gough DO, et al. 2010. *Astron. Astrophys. Rev.* 18:197
- Asplund M, Grevesse N, Sauval AJ, Scott P. 2009. *Annu. Rev. Astron. Astrophys.* 47:481
- Baby LT, Bordeanu C, Goldring G, Hass M, Weissmann L, et al. 2003a. *Phys. Rev. C* 67:065805
- Baby LT, Bordeanu C, Goldring G, Hass M, Weissmann L, et al. 2003b. *Phys. Rev. Lett.* 90:022501
- Bahcall JN. 1964. *Phys. Rev. Lett.* 12:300
- Bahcall JN. 1989. *Neutrino Astrophysics*. Cambridge, UK: Cambridge Univ. Press
- Bahcall JN, Bahcall NA, Shaviv G. 1968. *Phys. Rev. Lett.* 20:1209
- Bahcall JN, Cabibbo N, Yahil A. 1972. *Phys. Rev. Lett.* 28:316
- Bahcall JN, Davis R Jr. 1982. In *Essays in Nuclear Astrophysics*, ed. CA Barnes, DD Clayton, D Schramm, pp. 243–85. Cambridge, UK: Cambridge Univ. Press
- Bahcall JN, Fowler WA, Iben I, Sears RL. 1963. *Ap. J.* 1237:344
- Bahcall JN, Krastev PI, Smirnov AY. 1998. *Phys. Rev. D* 58:096016
- Bahcall JN, Peña-Garay C. 2003. *J. High Energy Phys.* 11:004
- Bahcall JN, Pinnsoneault MH. 1995. *Rev. Mod. Phys.* 67:781
- Bahcall JN, Pinsonneault MH. 1992. *Rev. Mod. Phys.* 64:885
- Bahcall JN, Serenelli AM, Pinsonneault M. 2004. *Ap. J.* 614:464
- Baraffe I, Chabrier G. 2010. *Astron. Astrophys.* 521:A44

- Basu S, Antia HM. 1997. *MNRAS* 287:189
- Basu S, Antia HM. 2004. *Ap. J.* 606:L85
- Basu S, Chaplin WJ, Elsworth Y, New R, Serenelli AM. 2009. *Ap. J.* 699:1403
- Beeck B, Collet R, Steffen M, Asplund M, Cameron RH, et al. 2012. *Astron. Astrophys.* 539:A121
- Bethe HA. 1986. *Phys. Rev. Lett.* 56:1305
- Bethe HA, Critchfield CL. 1938. *Phys. Rev.* 54:248–54
- Biggio C, Blennow M, Fernandez-Martinez E. 2009. *J. High Energy Phys.* 0908:090
- Blennow M, Ohlsson T, Snellman H. 2004. *Phys. Rev. D* 69:073006
- Bonetti R, Brogгинi C, Campajola L, Corvisiero P, D’Alessandro A, et al. 1999. *Phys. Rev. Lett.* 82:5205
- Borexino Collab., Alimonti G, Arpesella C, Back H, Balata M, Bartolomei D, et al. 2009. *Nucl. Instrum. Methods A* 600:568
- Borexino Collab., Bellini G, Benziger J, Bonetti S, Buizza Avanzini B, Caccianiga L, et al. 2010. *Phys. Rev. D* 82:033006
- Borexino Collab., Bellini G, Benziger J, Bick D, Bonetti S, Bonfini G, et al. 2011. *Phys. Rev. Lett.* 107:141302
- Borexino Collab., Bellini G, Benziger J, Bick F, Bonetti S, Bonfini G, et al. 2012a. *Phys. Rev. Lett.* 108:051302
- Borexino Collab., Bellini G, Benziger J, Bick D, Bonetti S, Bonfini G, et al. 2012b. *Phys. Lett. B* 707:22
- Broggini C, Bemmerer D, Guglielmetti A, Menegazzo R. 2010. *Annu. Rev. Nucl. Part. Sci.* 60:53–73
- Caffau E, Ludwig H-G, Bonifacio P, Faraggiana R, Steffen M, et al. 2010. *Astron. Astrophys.* 514:A92
- Caffau E, Ludwig H-G, Steffen M, Ayres TR, Bonifacio P, et al. 2008. *Astron. Astrophys.* 488:1031
- Caffau E, Maiorca E, Bonifacio P, Faraggiana R, Steffen M, et al. 2009. *Astron. Astrophys.* 498:877
- Cameron AGW. 1958. *Annu. Rev. Nucl. Sci.* 8:299
- Castellani V, Degl’Innocenti S, Fiorentini G, Lissia M, Ricci B. 1994. *Phys. Rev. D* 50:4749
- Castro M, Vauclair S, Richard O. 2007. *Astron. Astrophys.* 463:755
- Chaplin WJ, Miglio A. 2013. *Annu. Rev. Astron. Astrophys.* 51:353–92
- Chen HH. 1985. *Phys. Rev. Lett.* 55:1534
- Chen M. 2006. *AIP Conf. Proc.* 944:25
- Christensen-Dalsgaard J. 2002. *Rev. Mod. Phys.* 74:1073
- Davis R Jr. 1955. *Phys. Rev.* 97:766
- Davis R Jr. 1964. *Phys. Rev. Lett.* 12:303
- Davis R Jr, Harmer DS, Hoffman KC. 1968. *Phys. Rev. Lett.* 20:1205
- Daya Bay Collab., An FP, Bai JZ, Balantekin AB, Band HR, Beavis D, et al. 2012. *Phys. Rev. Lett.* 108:171803
- Dilke JFWW, Gough DO. 1972. *Nature* 240:262
- Double Chooz Collab., Abe Y, Aberle C, Akiri T, dos Anjos JC, Ardellier F, et al. 2012. *Phys. Rev. Lett.* 108:131801
- Duebner FL, Gough D. 1984. *Annu. Rev. Astron. Astrophys.* 22:593
- Elliott JR, Kosovichev AG. 1998. *Ap. J.* 500:L199
- Faulkner J, Gilliland RL. 1985. *Ap. J.* 299:994
- Filippone BW, Elwyn AJ, Davids CN, Koetke DD. 1983. *Phys. Rev. C* 28:2222
- Fogli GL, Lisi E, Marrone A, Montanino D, Palazzo A, Rotunno M. 2012. *Phys. Rev. D* 86:013012
- Fogli GL, Lisi E, Montanino D, Palazzo A. 2000. *Phys. Rev. D* 62:013002
- Forero DV, Tórtola M, Valle JWF. 2012. *Phys. Rev. D* 86:073012
- Fowler WA. 1958. *Ap. J.* 127:551
- Franco D. 2011. *Nucl. Phys. B Proc. Suppl.* 221:344
- GALLEX Collab., Anselmann P, Hampel W, Heusser G, Kiko J, Kirsten T, et al. 1992. *Phys. Lett. B* 285:376
- GALLEX Collab., Anselmann P, Hampel W, Heusser G, Kiko J, Kirsten T, et al. 1994. *Phys. Lett. B* 327:377
- GALLEX Collab., Hampel W, Handt J, Heusser G, Kiko J, Kirsten M, et al. 1999. *Phys. Lett. B* 447:127
- Gavrin VN, Gorbachev VV, Verentzenkin EP, Cleveland BT. 2010. (arXiv:1006.2103)
- Gell-Mann M, Ramond P, Slansky R. 1979. In *Supergravity*, ed. D Freedman, P van Nieuwenhuizen, p. 315. Amsterdam: North Holland
- Gizon L, Birch AC. 2005. *Living Rev. Solar Phys.* 2:6
- Gonzalez-Garcia MC, Maltoni M, Salvado J. 2010. *J. High Energy Phys.* 1005:072
- Grevesse N, Asplund M, Sauval AJ, Scott P. 2011. *Can. J. Phys.* 89:327
- Grevesse N, Sauval AJ. 1998. *Space Sci. Rev.* 85:161

- Grieb C, Barabanov I, Blackmon J, Champagne A, Chang Z, et al. 2011. *Nucl. Phys. Proc. Suppl.* 221:349
- Guillot T. 2005. *Annu. Rev. Earth Planet. Sci.* 33:493
- Guzik JA. 2006. In *Proc. SOHO 18/GONG 2006/HELAS I, Beyond the Spherical Sun*, ed. K Fletcher, MJ Thompson, ESA SP-624:17. Noordwijk, ESA
- Guzik JA, Mussack K. 2010. *Ap. J.* 713:1108
- Hammache F, Bogaert G, Aguer P, Angulo C, Barhoumi S, et al. 1998. *Phys. Rev. Lett.* 80:928
- Hammache F, Bogaert G, Aguer P, Angulo C, Barhoumi S, et al. 2001. *Phys. Rev. Lett.* 86:3985
- Hass M, Broude C, Fedoseev V, Goldring G, Huber G, et al. 1999. *Phys. Lett. B* 462:237
- Hata N, Bludman S, Langacker P. 1994. *Phys. Rev. D* 49:3622
- Hata N, Langacker P. 1994. *Phys. Rev. D* 48:2937
- Haxton WC. 1986. *Phys. Rev. Lett.* 57:1271
- Haxton WC. 1995. *Annu. Rev. Astron. Astrophys.* 33:459
- Haxton WC. 2010. *Annu. Rev. Nucl. Part. Sci.* 59:1
- Haxton WC, Lin W. 2000. *Phys. Lett. B* 486:263
- Haxton WC, Serenelli AM. 2008. *Ap. J.* 687:678
- Haxton WC, Zhang WM. 1991. *Phys. Rev. D* 43:2484
- Heeger K, Robertson RGH. 1996. *Phys. Rev. Lett.* 77:3720
- Holmgren HP, Johnston R. 1958. *Bull. Am. Phys. Soc. II* 3:26
- Holmgren HP, Johnston R. 1959. *Phys. Rev.* 113:1556
- Huang Y, Lanou R, Maris H, Seidel G, Sethumadhavan B, et al. 2008. *Astropart. Phys.* 30:1–11
- Jelley N, McDonald AB, Robertson RGH. 2009. *Annu. Rev. Nucl. Part. Sci.* 59:431
- Junghans AR, Mohrmann EC, Snover KA, Steiger TD, Adelberger EG, et al. 2002. *Phys. Rev. Lett.* 88:041101
- Junghans AR, Mohrmann EC, Snover KA, Steiger TD, Adelberger EG, et al. 2003. *Phys. Rev. C* 68:065803
- Junghans AR, Snover KA, Mohrmann EC, Adelberger EG, Buchmann L, et al. 2010. *Phys. Rev. C* 81:012801R
- Junker M, D'Alessandro A, Zavatarelli S, Arpesella C, Bellotti E, et al. 1998. *Phys. Rev. C* 57:2700
- Kaether F, Hampel W, Heusser G, Kiko J, Kirsten T. 2010. *Phys. Lett. B* 685:47
- Kajita T, Totsuka Y. 2001. *Rev. Mod. Phys.* 73:85–118
- Kamiokande Collab., Fukuda Y, Hayakawa T, Inoue K, Ishihara K, Ishino H, et al. 1996. *Phys. Rev. Lett.* 77:1683
- Kamiokande Collab., Hirata KS, Kajita T, Kifune T, Kihara K, Nakahata M, et al. 1989. *Phys. Rev. Lett.* 63:16
- KamLAND Collab., Abe S, Furuno K, Gando A, Gando Y, Ichimura K, et al. 2011. *Phys. Rev. C* 84:035804
- KamLAND Collab., Eguchi K, Enomoto S, Furuno K, Goldman J, Hanada H, et al. 2003. *Phys. Rev. Lett.* 90:021802
- KamLAND Collab., Gando A, Gando Y, Ichimura K, Ikeda H, Inoue K, et al. 2011. *Phys. Rev. D* 83:052002
- KATRIN Collab., Angrik J, Armbrust T, Beglarian A, Besserer U, Blümer J, et al. 2004. <http://bibliothek.fzk.de/zb/berichte/FZKA7090.pdf>
- Krastev PI, Smirnov AY. 1989. *Phys. Lett. B* 226:341
- Krauss A, Becker HW, Trautvetter HP, Rolfs C, et al. 1987. *Nucl. Phys. A* 467:273
- Kudomi N, Masataka K, Takahisa K, Yoshida S, Kume K, et al. 2004. *Phys. Rev. C* 69:015802
- Kuzmin VA. 1966. *Sov. Phys. J. Exp. Theor. Phys.* 22:1051
- Lande K. 2010. *Annu. Rev. Nucl. Part. Sci.* 59:21
- Lim CS, Marciano WJ. 1988. *Phys. Rev. D* 371:1368
- Loreti FN, Balantekin AB. 1994. *Phys. Rev. D* 50:4762
- Maki Z, Nakagawa M, Sakata S. 1962. *Prog. Theor. Phys.* 28:870
- McKinsey DN, Coakley K. 2005. *Astropart. Phys.* 22:355–368
- Melendez J, Asplund M, Gustafsson B, Yong D. 2009. *Ap. J.* 704:L66
- Mikheyev SP, Smirnov AY. 1985. *Sov. J. Nucl. Phys.* 42:913
- Mikheyev SP, Smirnov AY. 1986. *Nuovo Cimento* 9C:17
- MINOS Collab., Adamson P, Auty DJ, Ayres DS, Backhouse C, Barr G, et al. 2011. *Phys. Rev. Lett.* 107:181802
- Mohapatra R, Senjanovic G. 1980. *Phys. Rev. Lett.* 44:912
- Montalban J, Miglio A, Noels A, Grevesse N, di Mauro MP. 2004. *Proc. SOHO 14/GONG 2004: Helio- and Asteroseismology: Towards a Golden Future* SP-559:574, ESA, Noordwijk
- Nordlund A. 2009. (arXiv:0908.3479)

- Otten EW, Weinheimer C. 2008. *Rep. Prog. Phys.* 71:086201
- Parke SJ. 1986. *Phys. Rev. Lett.* 57:1275
- Parke SJ. 1995. *Phys. Rev. Lett.* 74:839
- Peña-Garay C, Serenelli AM. 2008. (arXiv:0811.2424)
- Pontecorvo B. 1946. *Chalk River Lab. Rep. PD-205*
- Pontecorvo B. 1967. *Zb. Eksp. Teor. Fiz.* 53:1717
- RENO Collab., Ahn JK, Chebotaryov S, Choi JH, Choi S, Choi Y, et al. 2012. *Phys. Rev. Lett.* 108:191802
- Rogers FJ, Nayfonov A. 2002. *Ap. J.* 576:1064
- SAGE Collab., Abazov AI, Anosov OL, Faizov EL, Gavrin VN, Kalikhov AV, et al. 1991. *Phys. Rev. Lett.* 67:3332
- SAGE Collab., Abdurashitov JN, Faizov EL, Gavrin VN, Gusev AO, Kalikhov AV, et al. 1994. *Phys. Lett. B* 328:234
- SAGE Collab., Abdurashitov JN, Gavrin VN, Gorbachev VV, Gurkina PP, Ibragimova TV, et al. 2009. *Phys. Rev. C* 80:015807
- Schafer A, Koonin SE. 1987. *Phys. Lett. B* 185:417
- Schechter J, Valle J. 1980. *Phys. Rev. D* 22:2227
- Schechter J, Valle J. 1982. *Phys. Rev. D* 25:774
- Serenelli A, Basu S. 2010. *Ap. J.* 719:865–72
- Serenelli AM. 2010. *Ap. Space Sci.* 328:13
- Serenelli AM, Basu S, Ferguson JW, Asplund M. 2009. *Ap. J.* 705:L123
- Serenelli AM, Haxton WC, Peña-Garay C. 2011. *Ap. J.* 743:24
- SNO Collab., Aharmim B, Ahmed SN, Anthony AE, Beier EW, Bellerive A, et al. 2005. *Phys. Rev. D* 72:052010
- SNO Collab., Aharmim B, Ahmed SN, Anthony AE, Barros N, Beier EW, et al. 2010. *Phys. Rev. C* 81:055504
- SNO Collab., Aharmim B, Ahmed SN, Anthony AE, Barros N, Beier EW, et al. 2012. *Phys. Rev. C*. Submitted (arXiv:1109.0763)
- SNO Collab., Ahmad QR, Allen RC, Andersen TC, Anglin JD, Bühler G, et al. 2001. *Phys. Rev. Lett.* 87:071301
- SNO Collab., Ahmad QR, Allen RC, Andersen TC, Anglin JD, Barton JC, et al. 2002. *Phys. Rev. Lett.* 89:011301
- Spergel DN, Press WH. 1985. *Ap. J.* 294:663
- Stonehill LC, Formaggio JA, Robertson RGH. 2004. *Phys. Rev. C* 69:015801
- Strieder F, Gialanella L, Gyürky G, Schümann F, Bonetti R, et al. 2001. *Nucl. Phys. A* 696:219
- Super-Kamiokande Collab. 2012. <http://www-sk.icrr.u-tokyo.ac.jp/sk/index-e.html>
- Super-Kamiokande Collab., Abe K, Hayato Y, Iida T, Ikeda M, Ishihara C, et al. 2011. *Phys. Rev. D* 83:052010
- Super-Kamiokande Collab., Cravens JP, Abe K, Iida T, Ishihara K, Kameda J, et al. 2008. *Phys. Rev. D* 78:032002
- Super-Kamiokande Collab., Fukuda S, Fukuda Y, Hayakawa T, Ichihara E, Ishitsuka M, et al. 2003. *Nucl. Instrum. Methods A* 501:418
- Super-Kamiokande Collab., Fukuda Y, Hayakawa T, Ichihara E, Inoue K, Ishihara J, et al. 1998. *Phys. Rev. Lett.* 81:1562
- Super-Kamiokande Collab., Hosaka J, Ishihara K, Kameda J, Koshio Y, Minamino A, et al. 2006. *Phys. Rev. D* 73:112001
- Super-Kamiokande Collab., Smy MB, Ashie Y, Fukuda S, Fukuda Y, Ishihara K, et al. 2004. *Phys. Rev. D* 69:011104(R)
- Super-Kamiokande Collab., Smy MB, et al. 2013. *Nucl. Phys. B - Proc. Suppl.* 235–236:49–54 T2K Collab., Abe K, Abgrall N, Ajima Y, Aihara H, Albert JB, et al. 2011. *Phys. Rev. Lett.* 107:041801
- White M, Krauss L, Gates E. 1993. *Phys. Rev. Lett.* 70:375
- Wolfenstein L. 1978a. *Phys. Rev. D* 17:2369
- Wolfenstein L. 1978b. *Phys. Rev. D* 20:2634
- Wuchterl G, Klessen RS. 2001. *Ap. J.* 560:L185
- Yanagida T. 1980. *Prog. Theor. Phys.* 64:1103



# Contents

An Unscheduled Journey: From Cosmic Rays into Cosmic X-Rays <i>Yasuo Tanaka</i> .....	1
Solar Neutrinos: Status and Prospects <i>W.C. Haxton, R.G. Hamish Robertson, and Aldo M. Serenelli</i> .....	21
Three-Dimensional Dust Radiative Transfer <i>Jürgen Steinacker, Maarten Baes, and Karl D. Gordon</i> .....	63
Cool Gas in High-Redshift Galaxies <i>C.L. Carilli and F. Walter</i> .....	105
The Dawn of Chemistry <i>Daniele Galli and Francesco Palla</i> .....	163
The CO-to-H <sub>2</sub> Conversion Factor <i>Alberto D. Bolatto, Mark Wolfire, and Adam K. Leroy</i> .....	207
Stellar Multiplicity <i>Gaspard Duchêne and Adam Kraus</i> .....	269
Solar Irradiance Variability and Climate <i>Sami K. Solanki, Natalie A. Krivova, and Joanna D. Haigh</i> .....	311
Asteroseismology of Solar-Type and Red-Giant Stars <i>William J. Chaplin and Andrea Miglio</i> .....	353
Modeling the Panchromatic Spectral Energy Distributions of Galaxies <i>Charlie Conroy</i> .....	393
Nucleosynthesis in Stars and the Chemical Enrichment of Galaxies <i>Ken'ichi Nomoto, Chiaki Kobayashi, and Nozomu Tominaga</i> .....	457
Coevolution (Or Not) of Supermassive Black Holes and Host Galaxies <i>John Kormendy and Luis C. Ho</i> .....	511



# ANNUAL REVIEWS

It's about time. Your time. It's time well spent.

## New From Annual Reviews:

### ***Annual Review of Statistics and Its Application***

Volume 1 • Online January 2014 • <http://statistics.annualreviews.org>

Editor: **Stephen E. Fienberg**, *Carnegie Mellon University*

Associate Editors: **Nancy Reid**, *University of Toronto*

**Stephen M. Stigler**, *University of Chicago*

The *Annual Review of Statistics and Its Application* aims to inform statisticians and quantitative methodologists, as well as all scientists and users of statistics about major methodological advances and the computational tools that allow for their implementation. It will include developments in the field of statistics, including theoretical statistical underpinnings of new methodology, as well as developments in specific application domains such as biostatistics and bioinformatics, economics, machine learning, psychology, sociology, and aspects of the physical sciences.

**Complimentary online access to the first volume will be available until January 2015.**

#### TABLE OF CONTENTS:

- *What Is Statistics?* Stephen E. Fienberg
- *A Systematic Statistical Approach to Evaluating Evidence from Observational Studies*, David Madigan, Paul E. Stang, Jesse A. Berlin, Martijn Schuemie, J. Marc Overhage, Marc A. Suchard, Bill Dumouchel, Abraham G. Hartzema, Patrick B. Ryan
- *The Role of Statistics in the Discovery of a Higgs Boson*, David A. van Dyk
- *Brain Imaging Analysis*, F. DuBois Bowman
- *Statistics and Climate*, Peter Guttorp
- *Climate Simulators and Climate Projections*, Jonathan Rougier, Michael Goldstein
- *Probabilistic Forecasting*, Tilmann Gneiting, Matthias Katzfuss
- *Bayesian Computational Tools*, Christian P. Robert
- *Bayesian Computation Via Markov Chain Monte Carlo*, Radu V. Craiu, Jeffrey S. Rosenthal
- *Build, Compute, Critique, Repeat: Data Analysis with Latent Variable Models*, David M. Blei
- *Structured Regularizers for High-Dimensional Problems: Statistical and Computational Issues*, Martin J. Wainwright
- *High-Dimensional Statistics with a View Toward Applications in Biology*, Peter Bühlmann, Markus Kalisch, Lukas Meier
- *Next-Generation Statistical Genetics: Modeling, Penalization, and Optimization in High-Dimensional Data*, Kenneth Lange, Jeanette C. Papp, Janet S. Sinsheimer, Eric M. Sobel
- *Breaking Bad: Two Decades of Life-Course Data Analysis in Criminology, Developmental Psychology, and Beyond*, Elena A. Erosheva, Ross L. Matsueda, Donatello Telesca
- *Event History Analysis*, Niels Keiding
- *Statistical Evaluation of Forensic DNA Profile Evidence*, Christopher D. Steele, David J. Balding
- *Using League Table Rankings in Public Policy Formation: Statistical Issues*, Harvey Goldstein
- *Statistical Ecology*, Ruth King
- *Estimating the Number of Species in Microbial Diversity Studies*, John Bunge, Amy Willis, Fiona Walsh
- *Dynamic Treatment Regimes*, Bibhas Chakraborty, Susan A. Murphy
- *Statistics and Related Topics in Single-Molecule Biophysics*, Hong Qian, S.C. Kou
- *Statistics and Quantitative Risk Management for Banking and Insurance*, Paul Embrechts, Marius Hofert

Access this and all other Annual Reviews journals via your institution at [www.annualreviews.org](http://www.annualreviews.org).

**ANNUAL REVIEWS | Connect With Our Experts**

Tel: 800.523.8635 (US/CAN) | Tel: 650.493.4400 | Fax: 650.424.0910 | Email: [service@annualreviews.org](mailto:service@annualreviews.org)

